DESIGN OF FUEL OPTIMAL MANEUVERS

FOR MULTI-SPACECRAFT INTERFEROMETRIC IMAGING SYSTEMS

A Thesis

by

JAIME LUIS RAMIREZ RIBEROS

Submitted to the Office of Graduate Studies of
Texas A&M University
in partial fulfillment of the requirements for the degree of

MASTER OF SCIENCE

August 2006

Major Subject: Aerospace Engineering

DESIGN OF FUEL OPTIMAL MANEUVERS

FOR MULTI-SPACECRAFT INTERFEROMETRIC IMAGING SYSTEMS

A Thesis

by

JAIME LUIS RAMIREZ RIBEROS

Submitted to the Office of Graduate Studies of
Texas A&M University
in partial fulfillment of the requirements for the degree of

MASTER OF SCIENCE

Approved by:

Chair of Committee,   Suman Chakravorty
Committee Members,   John Junkins
                      David Hyland
                      Shankar Bhattacharyya
Head of Department,   Helen Reed

August 2006

Major Subject: Aerospace Engineering

ABSTRACT

Design of Fuel Optimal Maneuvers for

Multi-Spacecraft Interferometric Imaging Systems. (August 2006)

Jaime Luis Ramirez Riberos, B.S., Universidad de los Andes;

B.S., Universidad de los Andes

Chair of Advisory Committee: Dr. Suman Chakravorty

Multi-spacecraft interferometry imaging is an innovative concept intended to apply formations of satellites to obtain high resolution images allowing for the synthesis of a large size aperture through the combination of the signal from several sub-apertures. The design of such systems requires the design of trajectories that cover a specified region of the observation plane to obtain appropriate information to reconstruct an image of the source. A proposed configuration consists of symmetrical formations which use control thrust to actively follow spiral trajectories that would appropriately cover the specified regions. An optimization problem has to be solved to design the optimal trajectories with minimum fuel consumption. The present work introduces an algorithm to obtain near optimal maneuvers for multi-spacecraft interferometric imaging systems. Solutions to the optimization problem are obtained assuming the optimality of spiral coverage of the spatial frequency plane. The relationship between the error in the frequency content and the reliability of the image is studied to make a connection to the dynamics of the maneuver and define the parameters of the optimization problem. The solution to the problem under deep space dynamics is shown to be convex and is solved by discretization into a non-linear programing problem. Further, the problem is extended to include the effects of dynamical constraints and the effect of time varying relative position from the imaging system

to the target. For the calculation of the optimal trajectories, a two-stage hierarchical controller is proposed that obtains acceleration requirements of near minimum fuel maneuvers for different target-system configurations. Several cases are simulated to apply the algorithm. From the obtained results some conclusions about the feasibility and dynamical requirements of these systems are described.

To my parents and to Christina, the love of my life

ACKNOWLEDGMENTS

This thesis presents various stages of work developed during my master's studies at the Aerospace Department at Texas A&M University under the guidance of Dr. Suman Chakravorty. His advice and inciteful input spurred the development of the ideas for this work. I would like to offer my sincere thanks to him for all his support and direction on how to effectively conduct research while enjoying the process.

I would also like to extend thanks to the Aerospace Department at Texas A&M, especially Dr. Walter Haisler, Dr. Helen Reed and Karen Knabe, for their encouragement of young minds with big dreams who come from all over the world to find a supportive and welcoming environment.

I have also been very fortunate to have taken courses from a group of remarkable instructors including Dr. John Valasek, Dr. Johnny Hurtado, Dr. Rao Vadali and Dr. Shankar Battacharyya. Especially invaluable lessons were learned from distinguished professors Dr. John Junkins and Dr. David Hyland. The challenge of learning a portion of their inmense knowledge gave me inspiration.

Thanks to all my colleagues for their valuable help in and outside of the classroom, especially to Josh Davis, Mrinal Kumar and Iohan Ettohauti. I want to thank the many significant individuals in Colombia that have pushed me forward, especially my family, Jaime, Gilma and Sandra Ximena, for believing in me.

Last but not least, the unconditional support of Christina has been the most important influence on this acomplishment and many other goals.

TABLE OF CONTENTS

LIST OF TABLES

LIST OF FIGURES

FIGURE   Page

CHAPTER I

INTRODUCTION

The motivation for this research is the design of multi-spacecraft interferometric imaging systems (MSIIS) for the high resolution imaging of earth and space based targets. The main purpose of the present work is the design of near minimum fuel trajectories to study the relationship between the quality of a picture obtained by interferometric imaging using multiple spacecrafts and the dynamic requirements of the system.

An interferometric imaging system is a sparse aperture interferometric system that allows for the synthesis of a large size aperture through the combination of the signal from several sub-apertures, allowing for the formation of images with a resolution which is orders of magnitude better than that of a single telescope. [1]

Interferometric imaging falls under the category of long baseline interferometry, [2] that was first developed in the context of synthetic aperture radars (SAR), and has been successfully used in earth based astronomy [3]. The use of spacecraft formations for this purpose has been proposed and previous literature has dealt with the definition of the optical requirements and capacities of interferometric imaging systems aiming to obtain astronomical images, specifically, the imaging of extrasolar planets [4, 5, 6, 7]. Different techniques of interferometry using formations of separated spacecraft have been proposed, and their application to space-based targets have been studied. [8, 9]. The technological shortcomings of the optics of such systems are being overcome thanks to the improvement of computational systems and development of technologies which allow for better signal reception (resulting in higher Signal to Noise Ratios) and less stringent requirements on position control

---

The journal model is *IEEE Transactions on Automatic Control.*

and telemetry[10]. The dynamics and control of multi-spacecraft systems in orbital configurations has been a topic of considerable research, allowing for the design of robust and accurate trajectory control systems.[11, 12] Furthermore, the development of high specific impulse thrust systems has reduced the technological difficulties for satellite formations performing active tasks. However, the relationship between the dynamic requirements of the spacecraft in a formation and the image quality in active interferometric imaging tasks is far from being well studied.

Previous formation designs optimize the locations of the constituent telescopes such that some metric of image quality is optimized.[13, 14] These correspond to static optimization problems. However, for an MSIIS, due to the higher resolution requirements, the design variables are the trajectories of the constituent spacecraft. In order to assess the minimum requirements of these trajectories, a suitable optimization problem has to be posed. In previous work in this regard the dynamics of the spacecraft have been related to the Modulation Transfer Function (MTF) of the optical system and time/fuel optimal problems have been posed[15, 16, 17]. In [18], a heuristic approach considered the design of minimum fuel trajectories in the subset of spirals, subject to deep space dynamics, i.e. perturbation free dynamics, for distant planet imaging applications. However, when the corresponding problem is posed for formations in near-earth orbit the symmetry and other desirable features of the optimization problem in the case of deep space, such as convexity, disappear, and the structure of the problem does not allow for the design of a computationally efficient optimization method for the exact problem. Additionally, new optical and kinematic constraints arise, different from those studied in previous research.

This document contains some developments made on optimization algorithms for the computation of near minimum fuel maneuvers for multi-spacecraft imaging systems. The essence of this investigation is an optimization methodology for the de-

sign of near optimal trajectories that minimize fuel consumption for multi-spacecraft interferometric imaging systems for any number of spacecraft under dynamical constraints.

Solutions for the optimization problem are initially proposed considering quasi-static targets with the system subject to deep space dynamics, i.e. double integrator perturbation free dynamics. This kind of systems addresses applications where gravitational forces are negligible and the target is located at a far distance. A case of such a system is an extra-solar planet imager located at a Lagrange point.

The solution is then extended to the case when the system is subject to gravitational dynamical constraints. This is the case when differential gravitational forces are included assuming Clohessy-Wiltshire dynamic equations of motion for an imaging system located in a near earth orbit. The particular application studied is a GEO located system imaging earth based objects.

There are other scenarios that cannot be considered in the cases mentioned above because the relative position of the system to the target varies significantly over the time of the maneuver. Thus, the methodology is further extended to consider cases where the relative position of the target to the imaging system is varying in time. Particular cases in this category include a LEO located system imaging a GEO based target, or earth based targets being imaged from a non GEO location. The various particular applications are considered.

The outline of the document is as follows:

The second chapter of the document examines the principle of synthetic aperture imaging, and the relationship of the trajectories to the error in the process. The optimization problem to be solved for the design of multi-spacecraft imaging systems is stated at the end of the chapter. In the third chapter, the error in the frequency content of the image is related to the error in the reconstructed image in order to

define a metric of reliability of the final estimate and set limits in the frequency error second moment. Thus, a direct connection between the reliability of the image and the trajectories of the spacecraft is found. Two different metric of the reliability are considered. First, the pixelwise probability of bounded error, and second, the probability of a bounded total picture error. For the calculations, two types of interferometry are considered: direct interferometry and entry pupil interferometry. In the fourth chapter, the design of the systems under deep space dynamics is considered, and a direct optimization method is proposed, given the desirable characteristics of the dynamic system. As an application, the algorithm is applied to design systems for extrasolar planet imaging. The characteristics of the solutions are examined and the feasibility of such missions analyzed. In the fifth chapter, the optimization problem is considered with linear dynamics, specifically, the case of Clohessy-Wiltshire dynamic equations. In this case a direct optimization is not feasible, and a new solution algorithm consisting of a two stage hierarchical controller is proposed. In this algorithm, an outer loop finds solutions under deep space dynamics, and an inner LQ controller loop tracks the trajectories found in the first stage to satisfy the coverage constraints. The solutions using the algorithm are applied for a particular application, an IR earth imager located in GEO, and the solutions and some characteristics of the results are displayed. In the sixth chapter, the problem is extended to the case when the distance and the direction to the target are time-varying. A new cost function has to be defined and terms that had been initially neglected in the approximation to the cost function for deep space in the second chapter, have to be considered. The effect of the change of direction of the optical axis is considered, as well as the effects caused by the time varying relative distance from the imaging system to the target. In this case, the main interests is the study of the dynamics of the maneuver for different combinations of orbits and targets. In this tool Lagrange Generating Functions are

used to define the positions for any time in the maneuver and calculate the relative distance and rotation angles of the relative frames, as well as their rates, as functions of time which are then given as an input to the design algorithm. Different cases are simulated and their results are shown: an imaging system located in LEO obtaining images from targets in different LEO orbits, MEO and GEO orbits as well as a case when imaging an earth based target.

CHAPTER II

MULTI-SPACECRAFT IMAGING

In this chapter the development of the equations defining the multi-spacecraft process is briefly described. These results are more extensively developed in Refs.[5, 6, 2], with slightly differences in the development. In this document a more general approach is presented and the spiral trajectories optimization problem is extended to any number of spacecraft.

A.   Basics of Interferometric Imaging

Interferometric imaging consists of reconstructing an image from measurements of light interference[2]. An imaging process consists essentially of reconstructing the intensity of a source at a different location. One common way to do this imaging process is using lenses or analog optical instruments. The lenses converge the signal from the source at a given plane, and the record of the signal intensity at every point of that plane is what is seen as an image. Fig 1, shows an illustration of this process.

   However, the development of digital systems allows for the reproduction of this process without the need of lenses. The physics of the lenses can be essentially simulated through a computer and the image reconstructed. If instead of a lens, a collection of devices being able to record the information of the electric field at different points of a surface is used, the configuration of a source that causes such pattern in the electric field could then be calculated.

   The electromagnetic field transports the information of the source in the form of electromagnetic waves. The electromagnetic waves are a solution to the Maxwell
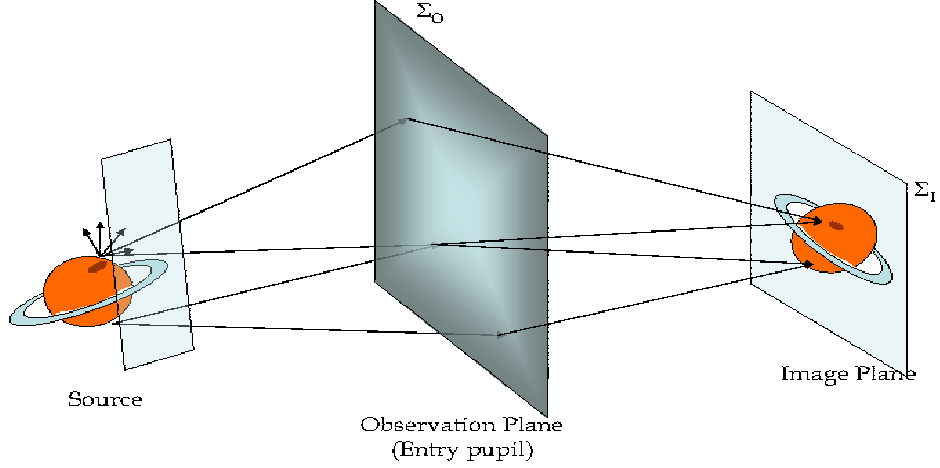
Fig. 1. Image formation process

equations [19]:

$$\nabla^2 \mathbf{E} = \frac{1}{c^2} \frac{\partial^2 \mathbf{E}}{\partial t^2} \tag{2.1}$$

$$\nabla \cdot \mathbf{E} = 0 \tag{2.2}$$

where c is the speed of the wave.

A solution to this equation, is a plane wave along the x direction:

$$\mathbf{E}(\mathbf{x}, t) = \hat{\mathbf{s}} E_o \exp(i(-\omega t \pm \mathbf{k} \cdot \mathbf{x} + \phi)) \tag{2.3}$$

where $\frac{\omega}{k} = c$.

The polarization of the light is not taken into account for the analysis. The analysis will hold for any transversal component of the wave, i.e. any vector $\hat{s}$, and therefore, we can define a scalar component of the field $U(x, t)$ that defines the behavior of the field along the x axis:

$$U(\mathbf{x}, t) = E_o e^{-i\phi} \exp(i(-\omega t \pm \mathbf{k} \cdot \mathbf{x})), \tag{2.4}$$

whose fourier transform is:

$$\hat{U}(\mathbf{x}, \omega) = \int_{-\infty}^{\infty} U(\mathbf{x}, t) \exp(-i\omega t) dt, \tag{2.5}$$

if a narrow bandwidth of detection $\Delta\omega$ is assumed, U can be described by the average value of the field over a very small variation of the frequency around the average frequency $\Delta\omega$, such that

$$U(\mathbf{x}) = \bar{U}(\mathbf{x}, \bar{\omega}). \tag{2.6}$$

Then, the fourier transform of the spatial distribution of this time independent function:

$$\hat{U}(\mathbf{u}) = \int_{-\infty}^{\infty} \int_{-\infty}^{\infty} E(\mathbf{x}) \exp(-i2\pi \mathbf{u} \cdot \mathbf{x}) dx dy \tag{2.7}$$

is a solution to Helmholtz equation.

By superposition of the solutions to the Helmholtz equation assuming a point source, the field at a point $\mathbf{r}$ can be written as caused by a distribution of sources located over the $z = 0$ plane as:

$$\hat{U}(\mathbf{r}, \bar{\omega}) = \frac{-i\bar{k}}{2\pi} \int_{\infty}^{\infty} \sigma(\mathbf{r}')\hat{s} \cdot \hat{z} \frac{\exp(i\bar{k}r)}{r} d\mathbf{r}' \tag{2.8}$$

where $\sigma(x)$ is the distribution function of the sources.

1. The Huygens Fresnel Principle

The equation 2.8 can be used to calculate the field at any point P as a combination of the distributions on an infinite surface Σ_I, called the image plane, propagating the light waves forward in time. This is known as the Huygens-Fresnel Principle (HFP)

and the a more general derivation can be written as:

$$U(\mathbf{P}, \bar{\omega}) \cong \frac{-i\bar{k}}{2\pi} \int_{\Sigma_I} (\hat{n}_Q \cdot \hat{s}_Q) \frac{e^{i\bar{k}r}}{r} U(\mathbf{Q}) d\mathbf{Q} \tag{2.9}$$

where $\hat{n}_Q$ is a vector perpendicular to the surface Σ_I, and $\hat{s}_Q$ is the vector from the source to the point Q.

Correspondingly the Inverse HFP, allows for the calculation of the distribution of the field at a point Q as a function of the field distribution on a different surface, Σ_o (the observation surface), by propagating the light waves backward in time:

$$U(\mathbf{Q}, \bar{\omega}) \cong \frac{-i\bar{k}}{2\pi} \int_{\Sigma_o} (\hat{n}_P \cdot \hat{s}_P) \frac{e^{-i\bar{k}r}}{r} U(\mathbf{P}) d\mathbf{P} \tag{2.10}$$

The fourier transforms of these equations are:

$$U(\mathbf{P}, t) = \int_{-\infty}^{\infty} U(\mathbf{P}, \bar{\omega}) e^{-i\omega t} dt \tag{2.11}$$

$$= \frac{-ik}{2\pi} \int_{\Sigma_I} (\hat{n}_Q \cdot \hat{s}_Q) \frac{1}{r} U(\mathbf{Q}, t - r/c) d\mathbf{Q}, \tag{2.12}$$

and, conversely, for the Inverse FHP:

$$U(\mathbf{Q}, t) = \frac{ik}{2\pi} \int_{\Sigma_o} (\hat{n}_P \cdot \hat{s}_P) \frac{1}{r} U(\mathbf{P}, t + r/c) d\mathbf{P} \tag{2.13}$$

B.   Mutual Coherence

It is now useful to define the concept of mutual coherence and complex degree of coherence. The mutual coherence function of a field $u(\mathbf{x}, t)$ is defined as [2]:

$$\mathbf{\Gamma}_{12}(\tau) = \langle u(\mathbf{P_1}, t + \tau), u^*(\mathbf{P_2}, t) \rangle, \tag{2.14}$$

and represents the spatial-temporal cross-correlation function of the light from two points, $\mathbf{P_1}$, $\mathbf{P_2}$. When dealing with a quasi-monochromatic signal, the coherence can

be approximated as [2]:

$$\boldsymbol{\Gamma_{12}}(\tau) \cong \mathbf{J}_{12}e^{-2\pi i\bar{\nu}\tau}, \tag{2.15}$$

where:

$$\mathbf{J}_{12} = \Gamma_{12}(0) = \langle u(\mathbf{P_1}, t), u^*(\mathbf{P_2}, t) \rangle \tag{2.16}$$

is the *mutual intensity.*

Now, if the mutual coherence of the field is calculated for two points in the observation surface Q_1, Q_2:

$$\boldsymbol{\Gamma}(\mathbf{Q_1}, \mathbf{Q_2}; \tau) = \langle u(\mathbf{Q_1}, t+\tau), u^*(\mathbf{Q_2}, t) \rangle \tag{2.17}$$

where, from the FHP:

$$u(\mathbf{Q_1}, t+\tau) = \frac{1}{i\bar{\lambda}} \iint_{\Sigma_I} \frac{1}{r_1}\mathbf{u}\left(\mathbf{P_1}, t+\tau - \frac{r_1}{c}\right)\chi(\theta_1)d\mathbf{Q_1} \tag{2.18}$$

$$u(\mathbf{Q_1}, t) = \frac{-1}{i\bar{\lambda}} \iint_{\Sigma_I} \frac{1}{r_2}\mathbf{u}^*\left(\mathbf{P_2}, t - \frac{r_2}{c}\right)\chi(\theta_2)d\mathbf{Q_2} \tag{2.19}$$

and $\chi(\theta_i) = \hat{n}_{P_i} \cdot \hat{s}_{P_i}$ is:

$$\boldsymbol{\Gamma}(\mathbf{Q_1}, \mathbf{Q_2}; \tau) = \iint_{\Sigma_I} \iint_{\Sigma_I} \frac{1}{\lambda^2 r_1 r_2}\boldsymbol{\Gamma}\left(\mathbf{P_1}, \mathbf{P_2}; \tau + \frac{r_2 - r_1}{c}\right)\chi(\theta_1)\chi(\theta_2)d\mathbf{Q_1}d\mathbf{Q_2} \tag{2.20}$$

then, the mutual intensity is:

$$\mathbf{J}(\mathbf{Q_1}, \mathbf{Q_2}) = \boldsymbol{\Gamma}(\mathbf{Q_1}, \mathbf{Q_2}; 0) \tag{2.21}$$

$$= \iint_{\Sigma_I} \iint_{\Sigma_I} \frac{1}{\lambda^2 r_1 r_2}\boldsymbol{\Gamma}\left(\mathbf{P_1}, \mathbf{P_2}; \frac{r_2 - r_1}{c}\right)\chi(\theta_1)\chi(\theta_2)d\mathbf{Q_1}d\mathbf{Q_2} \tag{2.22}$$
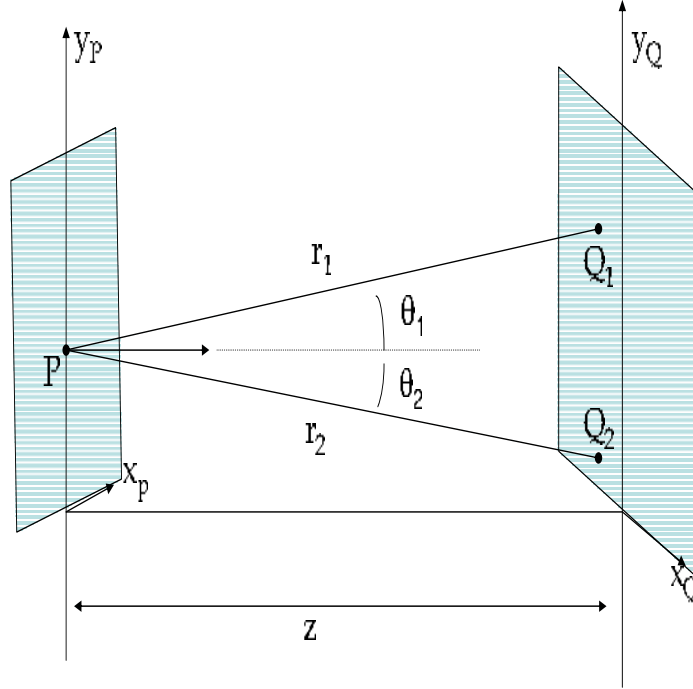
Fig. 2. Optical transfer function for a pair of circular telescopes

and the intensity at the point $\mathbf{Q}$:

$$\mathbf{I}(\mathbf{Q}) = \iint_{\Sigma_I} \iint_{\Sigma_I} \frac{1}{\lambda^2 r_1 r_2} \mathbf{J}(\mathbf{P_1}, \mathbf{P_2}) e^{-ik(r_2 - r_1)} \chi(\theta_1) \chi(\theta_2) d\mathbf{Q_1} d\mathbf{Q_2}$$

$$(2.23)$$

Given the geometry shown in Fig. 2, and the fact that $z \gg x$, $z \gg y$, the following approximations are valid:

$$r = \sqrt{z^2 + x_Q^2 + y_Q^2 - 2x_Q x_P - 2y_Q y_P} \qquad (2.24)$$

$$\cong z \left[1 + \frac{x_Q^2 + y_Q^2}{2z^2} + \frac{x_Q x_P + y_Q y_P}{z^2} \right] \qquad (2.25)$$

$$\chi(\theta_1) \cong \chi(\theta_1) \cong 1 \qquad (2.26)$$

$$\bar{\lambda} r_1 = \bar{\lambda} r_2 = \bar{\lambda} \bar{z} \qquad (2.27)$$

Thus, the intensity at $\mathbf{Q}$ can be written as:

$$\mathbf{I}(\mathbf{Q}) = \frac{1}{(\bar{\lambda}\bar{z})^2} \iint_{\Sigma_I} \iint_{\Sigma_I} \mathbf{J}(x_1, y_1; x_2, y_2) e^{\frac{2\pi i}{\bar{\lambda}\bar{z}}[(x_2-x_1)x_Q + (y_2-y_1)y_Q]} dx_1 dy_1 dx_2 dy_2$$

(2.28)

C. Sparse Aperture Systems

In a sparse aperture system, the observation surface is composed of several sub-apertures. The final image is formed by the addition of the signals from every pair of singular apertures, at every infinitesimal instant of time:

$$I = \int_0^T \sum_n \sum_m I_{nm}(t) dt$$

(2.29)

The intensity at a point $Q = (u, v)$ of the image formed from a pair of receivers located at P_n, P_m, following the equations in the previous section is:

$$I_{nm}(x_Q, y_Q; t) = \frac{1}{\lambda^2 \bar{z}^2} \iiiint \mathbf{J}'(\sigma_n, \varsigma_n; \sigma_m, \varsigma_m) e^{\frac{2\pi i}{\bar{\lambda}\bar{z}}((\sigma_n-\sigma_m)y_Q + (\varsigma_n-\varsigma_m)y_Q)} d\sigma_n d\varsigma_n d\sigma_m d\varsigma_m$$

(2.30)

where x_n, y_n are the coordinates in the entrance pupil plane for the nth spacecraft.

The collectors have a finite extent and are not perfect transmitters of the signal, such that the actual detected mutual coherence is:

$$\mathbf{J}'(\sigma_n, \varsigma_n, \sigma_m, \varsigma_m) = \mathbf{P}^{nm}(r_n, r_m; \sigma_n, \varsigma_n)\mathbf{P}^{nm*}(r_n, r_m; \sigma_m, \varsigma_m)\mathbf{J}(\sigma_n, \varsigma_n, \sigma_m, \varsigma_m)$$

(2.31)

where $\mathbf{P}^{nm}(r_n, r_m; x, y)$ is the point spread function of the collector pair nm. For simplicity of notation it will be written as P^{nm}, being implicit that it depends on the positions of the spacecraft (r_n, r_m). This function accounts for the aberration and the

finite extension of the collectors.

The spatial fourier transform of the expression in eq. 1.45 is [2]:

$$
\begin{aligned}
\mathscr{I}_{nm}(\nu;t) &= \frac{1}{\lambda^2 \bar{z}^2} \iiiint_{\Sigma_I} d\sigma_n d\varsigma_n d\sigma_m d\varsigma_m \mathbf{J}'(\sigma_n, \varsigma_n; \sigma_m, \varsigma_m) \qquad (2.32) \\
&\times \iint dx_Q dy_Q e^{2\pi i \left[\left(\nu_u + \frac{\sigma_m - \sigma_n}{\lambda z} \right) x_Q + \left(\nu_v + \frac{\varsigma_m - \varsigma_n}{\lambda z} \right) y_Q \right]} \\
&= \frac{1}{\lambda^2 \bar{z}^2} \int_{\Sigma_I} d\sigma_n d\varsigma_n d\sigma_m d\varsigma_m \mathbf{J}'(\sigma_n, \varsigma_n; \sigma_m, \varsigma_m) \\
&\times \delta \left[\left(\nu_u + \frac{\sigma_m - \sigma_n}{\lambda z} \right); \left(\nu_v + \frac{\varsigma_m - \varsigma_n}{\lambda z} \right) \right] \qquad (2.33) \\
&= \int_{\Sigma_I} \mathbf{J}'\left(\sigma_n, \varsigma_n; \sigma_n - \lambda z \nu_u, \varsigma_n - \lambda z \nu_v \right) d\sigma_n d\varsigma_n \qquad (2.34) \\
&= \int_{\Sigma_I} \mathbf{J}'(r_n; r_n - \lambda z \nu) dS_n \qquad (2.35) \\
&= \int_{\Sigma_I} \mathbf{P}^{nm}(r_n) \mathbf{P}^{nm*}(r_n - \lambda z \nu) \mathbf{J}(r_n; r_n - \lambda z \nu) dS_n \\
&\qquad\qquad\qquad\qquad\qquad\qquad\qquad\qquad\qquad\qquad (2.36)
\end{aligned}
$$

where ν is the frequency vector (ν_u, ν_v).

Now we make use of the Fresnel-Huygens Principle to relate the measurements in the observation plane to the actual intensity of the source. Due to the fact that the source is conformed by incoherent sources of light ($J(P_n, P_m) = I(P_n)\delta_{nm}$), the mutual coherence is only a function of the separation of the observation points (VanCittern-Zernike Theorem), and thus (see ref. [2]):

$$
\begin{aligned}
\mathbf{J}(\Delta x, \Delta y) &= \frac{e^{i\psi}}{(\bar{\lambda}\bar{z})^2} \iint_{-\infty}^{\infty} I(\xi, \eta) e^{\frac{2\pi i}{\lambda z}(\Delta x \xi + \Delta y \eta)} d\xi d\eta \\
\psi &= \frac{\pi}{\lambda z} \left(x_1^2 + y_1^2 - x_2^2 + y_2^2 \right) \qquad (2.37)
\end{aligned}
$$

Replacing into Eq. 2.36:

$$\mathscr{I}_{nm}(\nu, t) = \int_{\Sigma_I} \mathbf{P}^{nm}(r_n) \mathbf{P}^{nm*}(r_n - \lambda z\nu) \frac{e^{i\psi}}{(\bar{\lambda}\bar{z})^2} \iint_{-\infty}^{\infty} I(\xi, \eta) e^{\frac{2\pi i}{\lambda z}(\lambda z\nu_u \xi + \lambda z\nu_v \eta)} d\xi d\eta dS_n$$

$$= I(\nu, t) \int_{\Sigma_I} \mathbf{P}^{nm}(r_n) \mathbf{P}^{nm*}(r_n - \lambda z\nu) \frac{e^{i\psi}}{(\bar{\lambda}\bar{z})^2} dS_n \tag{2.38}$$

$$\tag{2.39}$$

When, taking care of the normalization factor, and noticing that for the cases of interest when $z >> D$ $e^{i\psi} \approx 1$, we find that:

$$\mathscr{I}_{nm}(\nu; t) = \mathbf{I}_{nm}(\nu; t) \frac{A_{col}}{(\bar{\lambda}\bar{z})^2} \frac{\int_{\Sigma_I} \mathbf{P}^{nm}\left(\frac{r_n(t)}{\lambda z}\right) \mathbf{P}^{nm*}\left(\frac{r_n(t)}{\lambda z}; \frac{r_n(t)}{\lambda z} - \nu\right) dSn}{\int_{\Sigma_I} |\mathbf{P}^{nm}\left(\frac{r_n(t)}{\lambda z}\right)|^2 dS_n} \tag{2.40}$$

$$= \mathbf{I}(\nu; t) \mathbf{A}^{nm}(\nu, t) \tag{2.41}$$

where A_{col} is the area of collection, that in the case of non-abberrated aperture has the same value as the integral denominator in the above equation.

1. Noise in the Interferometric Process

The mutual coherence is an electromagnetic effect, and by nature is random due to the photogeneration process. Photons from an incoherent source are generated randomly following a Poisson distribution. The measuring process also inputs errors and uncertainties in the signal such that[5]:

$$\mathbf{J}_{nm}(Q; t) = \bar{\mathbf{J}}(Q) + \delta\mathbf{J}_{nm}(t) \tag{2.42}$$

where $\bar{\mathbf{J}}$ is the expected value over time of the mutual coherence, and $\delta\mathbf{J}_{nm}$ is a position independent, time-dependent random variable that accounts for the random variations and the noise in the measurements of the pair nm. Then, the measured

intensity is:

$$\mathscr{I}_{nm}(\nu;t) = \bar{\mathbf{I}}(\nu)\mathbf{A^{nm}}(\nu,t) + \delta\mathbf{J}_{nm}(t)\mathbf{A^{nm}}(t) \qquad (2.43)$$

where $\mathbf{A^{nm}}(\nu,t)$ is the time-dependent Optical Transfer Function:

$$\mathbf{A^{nm}}(\nu,t) = \frac{A_{col}}{(\bar{\lambda}\bar{z})^2} \frac{\int_{\Sigma_I} \mathbf{P}^{nm}\left(\frac{r_n(t)}{\lambda z}\right) \mathbf{P}^{nm*}\left(\frac{r_n(t)}{\lambda z}; \frac{r_n(t)}{\lambda z} - \nu\right) dSn}{\int_{\Sigma_I} |\mathbf{P}^{nm}\left(\frac{r_n(t)}{\lambda z}\right)|^2 dS_n}$$

$$(2.44)$$

and thus, the final image intensity at the end of the maneuver, given the measurements of each pair of spacecraft is:

$$\mathscr{I}(\nu) = \int_0^T \sum_n \sum_m \mathscr{I}_{nm}(\nu,t)dt \qquad (2.45)$$

$$= \bar{\mathbf{I}}(\nu_u,\nu_v) \int_0^T \sum_n \sum_m \mathbf{A^{nm}}(\nu,t)dt + \int_0^T \sum_n \sum_m \delta\mathbf{J}_{nm}(t)\mathbf{A^{nm}}(\nu,t)dt$$

$$(2.46)$$

In order to have a normalized value for $\mathscr{I}(\nu)$, we define the normalized intensity $i(\nu) = \frac{\mathscr{I}(\nu)}{I_{est}}$, where $I(0) = I_{est}$ is the mean intensity of radiation $n_s\Delta\nu e_\nu$.

Then, the expression for the reconstructed frequency plane content for a given imaging maneuver:

$$i(\nu) = M(\nu)\mathbf{I}(\nu) + N(\nu) \qquad (2.47)$$

being:

$$M(\nu) = \int_0^T \sum_n \sum_m \mathbf{A^{nm}}(\nu,t)dt \qquad (2.48)$$

$$N(\nu) = \frac{1}{I_{est}}\int_0^T \sum_n \sum_m \delta\mathbf{J}_{nm}(t)\mathbf{A^{nm}}(\nu,t)dt \qquad (2.49)$$

and ν is the frequency vector, (ν_u,ν_v).

2. The Aperture Function

As mentioned, the aperture function identifies the aberrations and finiteness of the pupil in the observation plane. For our purposes it is assumed that the telescopes have very low aberration, i.e. their pupil functions are real non-negative, and thus that the Optical Transfer Function is defined by its modulus, the pairwise time dependent Modulation Transfer Function. In this case, the aperture function is just the geometrical autocorrelation function given by the integral:

$$\mathbf{A}^{nm}(\nu,t) = \frac{1}{(\bar{\lambda}\bar{z})^2} \int_{\Sigma_I} \mathbf{P}^{nm}\left(\frac{r_n(t)}{\lambda z}\right) \mathbf{P}^{nm*}\left(\frac{r_n(t)}{\lambda z}; \frac{r_n(t)}{\lambda z} - \nu\right) dx_n dy_n$$

$$(2.50)$$

The autocorrelation function for a single circular pupil function is the function known as *witch hat*, and is shown in Fig. 3.

For a pair of circular telescopes, located at a relative distance Δr_{mn}, the optical transfer function is given by:

$$\mathbf{A^{nm}}(\nu) = \begin{cases} \frac{D_T^2}{2\lambda^2 z^2}(\cos^{-1}(1-\rho) - (1-\rho)\sqrt{2\rho-\rho^2}) & if \quad \rho \geq 0 \\ 0 & otherwise. \end{cases}$$

$$(2.51)$$

$$\rho = 1 - \left(\frac{\lambda z}{D_T}\right)\left|\nu - \frac{(\Delta r_{nm})}{\lambda z}\right|$$

$$(2.52)$$

The case for the Total Modulation Transfer Function for a pair of telescopes, taking into account the contributions of the pair nm and the pair mn is illustrated in Fig. 4.

When we integrate this function over time accounting for the relative trajectories of the telescopes, we have the Modulation Transfer Function (MTF), of the synthesized instrument, as is shown in Fig. 5.
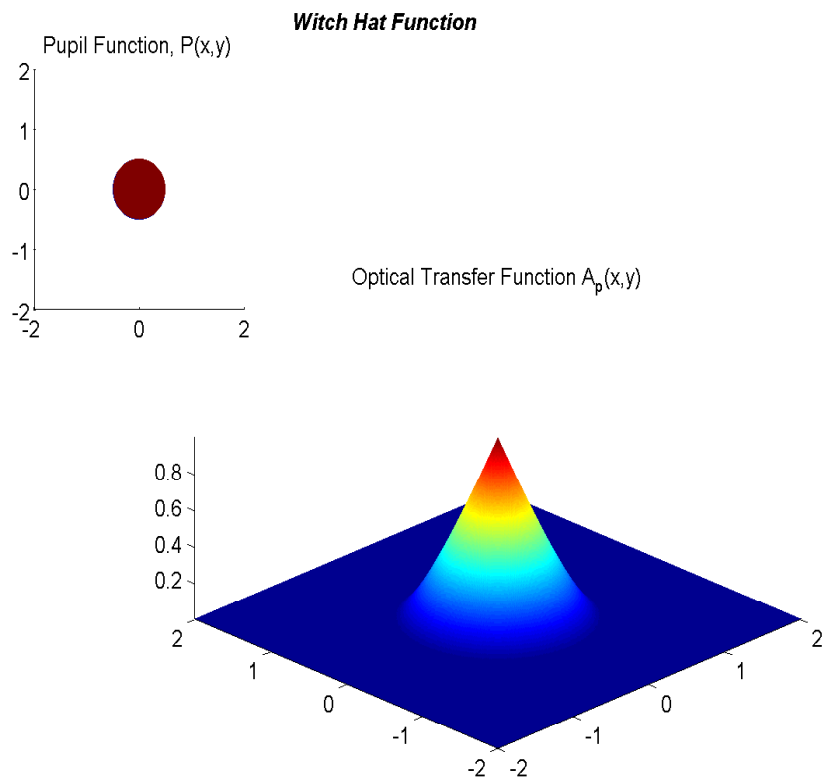
Fig. 3. Witch hat function - OPT for a unaberrated circular aperture
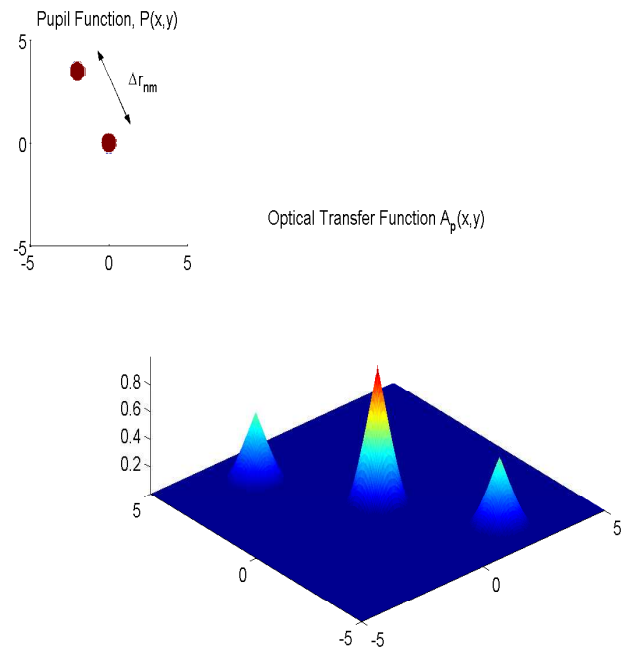
Fig. 4. Optical transfer function for a pair of circular telescopes
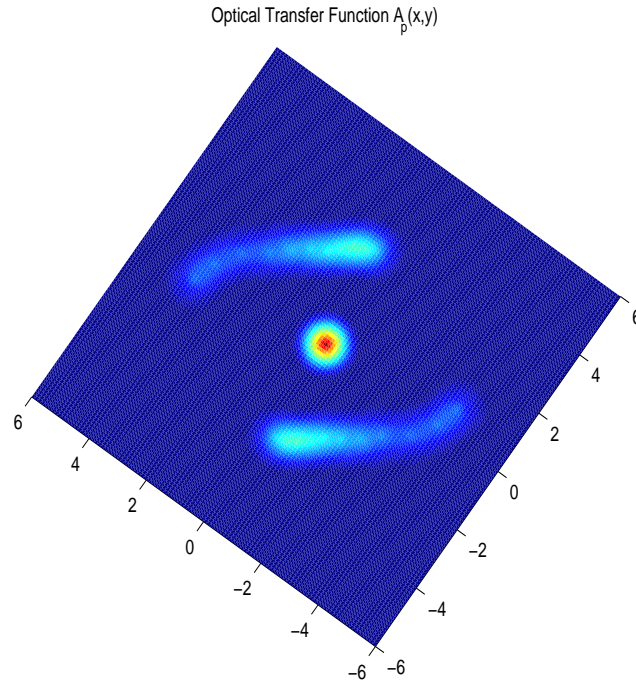
Fig. 5. Modulation transfer function for a moving pair of circular telescopes

D. Relationship Error - Kinematics

Using telemetric measurements of the positions of the spacecraft for any time it is possible reconstruct the MTF function given by Eq. 2.48, such that an (scaled) reconstruction of the frequency content is estimated:

$$\hat{i}(\nu) = M(\nu)^{-1} i(\nu) \tag{2.53}$$

$$= \bar{\mathbf{I}}(\nu) + M(\nu)^{-1} N(\nu) \tag{2.54}$$

$$= \bar{\mathbf{I}}(\nu) + e(\nu) \tag{2.55}$$

where the error is given by:

$$e(\nu) = \frac{N(\nu)}{M(\nu)} \tag{2.56}$$

such that the covariance of the error is given by [5]:

$$E|e(\nu)|^2 = E\left|\frac{N(\nu)}{M(\nu)}\right|^2 \tag{2.57}$$

$$= \frac{E|\int_0^T \sum_n \sum_m \delta\mathbf{J}_{nm}(t)\mathbf{A^{nm}}(t)dt|^2}{I_{est}^2|\int_0^T \sum_n \sum_m \mathbf{A^{nm}}(t)dt|^2} \tag{2.58}$$

where the value of $\delta\mathbf{J}_{nm}(t)$ depends on the interferometric process. Considering $\delta\mathbf{J}_{nm}(t)$ a random process with mean 0 and variance $\sigma_J^2(t)$ and given the fact that $\delta_{mn}^k(t)$ and $\delta_{mn}^l(t)$ are independent if $k \neq l$, and δ_{mn}^k and δ_{pq}^k, are independent too unless $m = p$ and $n = q$ or $m = q$ and $n = p$, and:

$$\mathbf{A}^{nm}\mathbf{A}^{mn} \approx 0 \tag{2.59}$$

we have that N is a summation of approximately independent random variables with variance $\sigma_J^2(t)$, and given the central limit theorem [5]:

$$var[N(\nu)] \quad = \quad \frac{\sigma_J^2 dT}{I_{est}^2} \sum_{k=1}^{L} \sum_n \sum_m |\mathbf{A}^{nm}(t)|^2 dt \qquad (2.60)$$

where dT is an infinitesimal time of collection.

Then

$$var[N(\nu)] \quad = \quad \frac{\sigma_J^2 dT}{I_{est}^2} \int_0^T \sum_n \sum_m |\mathbf{A}^{nm}(t)|^2 dt. \qquad (2.61)$$

For the pupil function assumed, the following approximation is valid:

$$|\mathbf{A}^{nm}(t)|^2 \approx |\mathbf{A}^{nm}(t)| \qquad (2.62)$$

such that the relationship between the error in the frequency plane and the dynamics of the spacecraft is given by:

$$E|e(\nu)|^2 \quad = \quad \frac{\sigma_J^2 dT}{I_{est}^2 \int_0^T \sum_n \sum_m \mathbf{A}^{nm}(t) dt} \qquad (2.63)$$

E.   Error Variance for Different Interferometric Methods

The relationship between the error in the frequency content and the trajectories of the spacecraft can be defined given the distribution of δJ_{mn}, whose variance depends on the type of interferometric process. The relationship is calculated for different techniques that could be used in these systems.

1. Direct Interferometry

In a direct interferometer, the light from the two spacecraft is directed to a combiner and interfered, and the amplitude and phase of the peak in the interfered signal is measured, giving the information of amplitude and phase of the mutual coherence at the relative positions of the spacecraft.

The variance of the real and imaginary components of the error of the mutual coherence measurement, δJ, are affected by the inherent stochastical behavior of the electromagnetic process and the noise caused by the thermal effects in the optics: [4, 3]:

$$\sigma^2[\delta J_{nm}(t)] = \left(1 + \frac{\kappa_o}{\tau_{opt} n_s}\right) \frac{\tau_{opt} e_\nu I_{est}}{A_{col} dT} \tag{2.64}$$

where

$$\kappa_o = \frac{1 - \epsilon}{\left(e^{h\nu/kT_{opt}} - 1\right)} \tag{2.65}$$

is the factor that accounts for the thermal noise of the detectors, ϵ is the fractional transmition of thermal energy, T_{opt} is the temperature of the optics, τ_{opt} is the optical efficiency, n_s is the density number of photons, e_ν is the energy of photons at frequency ν, A_{tot} is the area of collection and dT is the time of collection.

In direct interferometry, the signal cannot be amplified or manipulated in order to compensate for the optical effects of the mirrors that affect the total signal for the process. It has to be divided to interfere with the light of every other telescope so the final signal is divided by (M-1) and a term accounting for the optical efficiency ς has also to be included in the pupil function[7]. The actual MTF for a pair of spacecraft is multiplied by a factor $\frac{\sqrt{\varsigma}}{(M-1)}$.

Then, following from Eq. 2.63 the variance of the error is:

$$\sigma^2[e(\nu)] = \left(1 + \frac{\kappa_o}{\tau_{opt} n_s}\right) \frac{(M-1)^2}{\tau_{opt} \varsigma \mu_{tot} \int_0^T \sum_n \sum_m \mathbf{A}^{nm}(\nu, t) dt} \qquad (2.66)$$

where μ_{tot} is the total rate of photons per second acquired by the system.

2. Entry Pupil Interferometry

In entry pupil interferometry methods like heterodyne interferometry or intensity interferometry the measurements of the signal are made at the observation plane, and these measurements are later interfered offline[7, 3]. In heterodyne interferometry, the acquired signal is first interfered with a coherent signal from the local oscillator (LO) that allows reproducing a downlinked version of the acquired signal in the radio frequency wavelength. A signal in the radio frequency band can be transmitted, manipulated and later interfered, and so there is no need to have a combiner to directly interfere the light from the source and the signal can be compensated by the losses in the optics. Intensity Interferometry uses the method developed by the Hanbury-Brown-Twiss, obtaining the mutual coherence intensity from the second order variations of the signal. In this case measurements of the Intensity are used to calculate the amplitude, but the phase is not directly measured and require the implementation of phase reconstruction methods, that require apriori knowledge of certain characteristics of the image.

These two methods introduce uncertainty noise on the signal[7]. For practical purposes, the noise and signal of the Intensity Interferometry behave similarly to the heterodyne interferometric process. The variance in error of the mutual coherence, δJ, for this technique [7] is:

$$\sigma^2[\delta J_{nm}] = \left(1 + \frac{1}{n_s} + \frac{\kappa_o}{n_s}\right) \frac{e_\nu I_{est}}{A_{col} dT} \qquad (2.67)$$

Then, from Eq. 2.63, it is found that the variance of the error in the frequency plane is:

$$\sigma^2[e(\nu)] \;=\; \left(1 + \frac{1}{n_s} + \frac{\kappa_o}{n_s}\right) \frac{1}{\mu_{tot} \int_0^T \sum_n \sum_m \mathbf{A}^{nm}(\nu, t)dt} \tag{2.68}$$

F. The Fuel Optimization Problem

When the purpose is to obtain knowledge of the minimum fuel consumption of this type of systems, it is necessary to formulate an optimization problem. The cost function of such optimization problem minimize a quantity proportional to the control required to follow the trajectories, and the solution is subject to the constraints of the problem given the dynamics, and the time and image requirements of the problem.

When constraining the minimum value of the error in the frequency plane derived from (2.66) or (2.68), we define a coverage constraint. That constraint defines the fact that the time spent covering a given area of the u-v plane has to be greater that a given lower bound in order to have appropriate coverage. So, given a bound for the maximum value of $\sigma^2[e]$, we can define a $\bar{\Delta}$ such that:

$$\int_0^T \sum_n \sum_m \mathbf{A^{nm}}(\nu, t)dt \geq \bar{\Delta} \tag{2.69}$$

The coverage of the witch hat functions, as shown in Fig. 6, can be approximated to a top hat function:

$$\mathbf{A}^{nm}(\nu, t) \;\approx\; \hat{A}_p\left(\nu - \frac{\Delta r_{nm}(t)}{\lambda z}\right), \tag{2.70}$$

$$\hat{A}_p(x) \;=\; \begin{cases} 1 & if \qquad\qquad ||x|| \leq \rho \\ 0 & otherwise. \end{cases} \tag{2.71}$$

Approximation of Witch hat to a cylindrical function
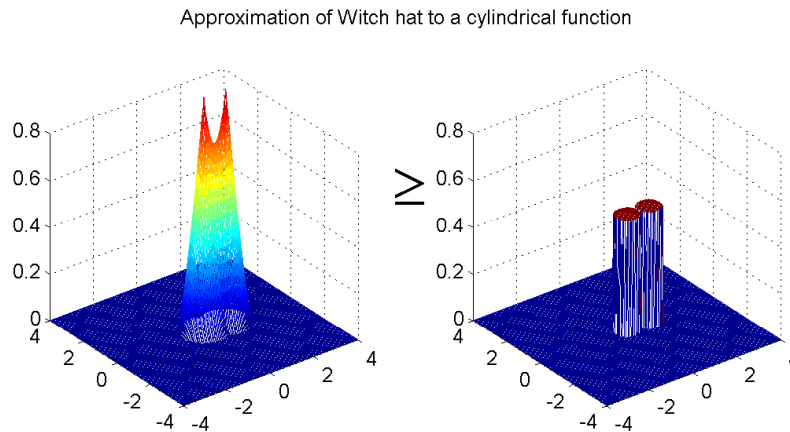
Fig. 6. Approximation of the witch hat function to a cylindrical function

In figure 6, the validity of the approximation is illustrated. The coverage of the unitary discs with a diameter at least of the hat define an appropriate lower bound for the addition of witch hats. Notice that both functions approximate to a delta function as the radius becomes smaller.

Then the coverage problem can be seen as a painting problem, where the discs are paintbrushes painting the uv plane, leaving a layer of paint proportional to the time spent on a given location [4]. This process is illustrated in Fig. 7. The size of the brushes is given by the size of the transform in the u-v plane of the telescope aperture, and the positions of the discs correspond to the relative distances of every pair of telescopes. A pair of telescopes has a footprint in the u-v plane, as shown in Fig. 7. Then the imaging problem consists of finding the trajectories of the spacecraft such that the discs defined by the u-v support function cover each point on the u-v plane for a minimum given amount of time.

The importance of a good coverage is presented in Fig. 8, where the reconstruc-
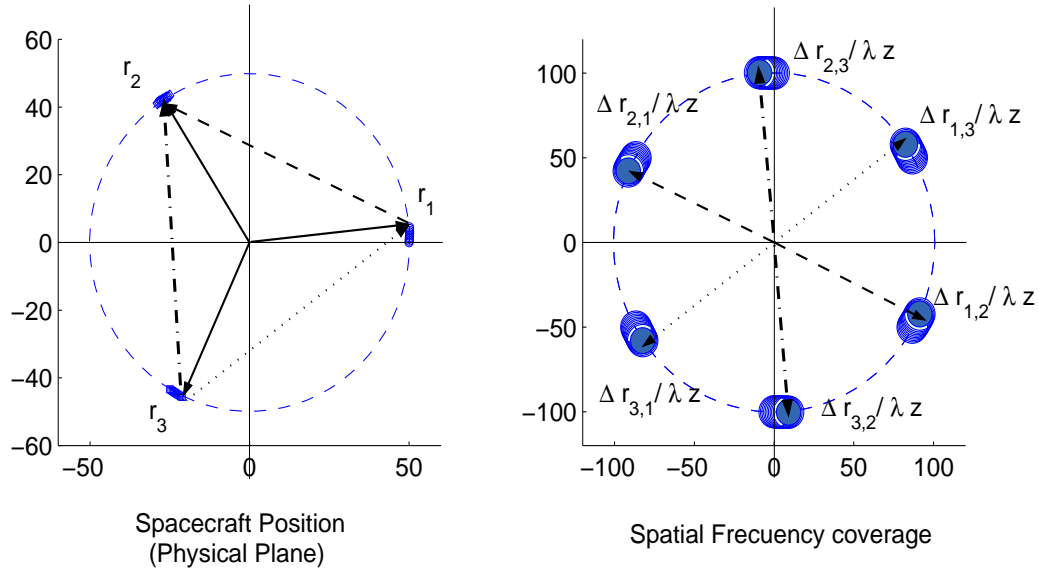
Fig. 7. Relationship between spacecraft positions and the spatial frequency coverage

tion of image is simulated for two different cases. In the first one, every region of the support in the u-v plane is covered long enough such that the error is low for every point. In the other case, all the support of the frequency plane is also covered, but in this case some regions are appropriately covered, whereas others are covered for a shorter amount of time, the error is greater, and hence, the image is not reconstructed with the required accuracy. Notice that in the second picture even if the noise in the inner and outer regions is much smaller than in the first picture, having a poorly covered region reduces the quality. Thus, active control is required for a complete and appropriate coverage of the u-v plane when time and image quality are constrains.

1.   Spiral Maneuvers

In order to define trajectories that achieve appropriate trajectories in the u-v plane, it is necessary to resort to heuristics. It has been shown [18] that due to the complexity of the general optimization problem is required to reduce the search set. The subset

Noise in MTF
$\sigma^2[e] = 0.3$

Reconstructed Image 1

Reconstructed Image 2

Noise in MTF

$\sigma^2[e] = 0.05$ $\sigma^2[e] = 2$

Reconstructed Image 1

Reconstructed Image 2
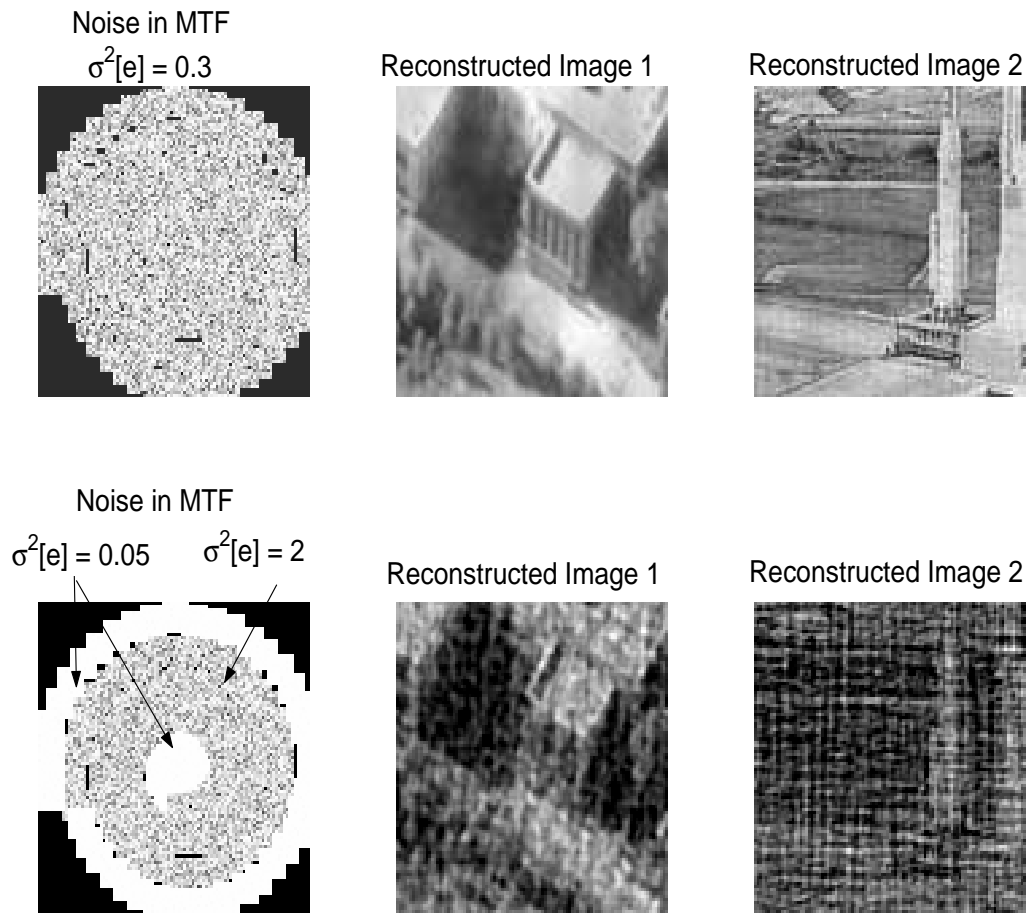
Fig. 8. Reconstructed images for different noise level in the u-v plane
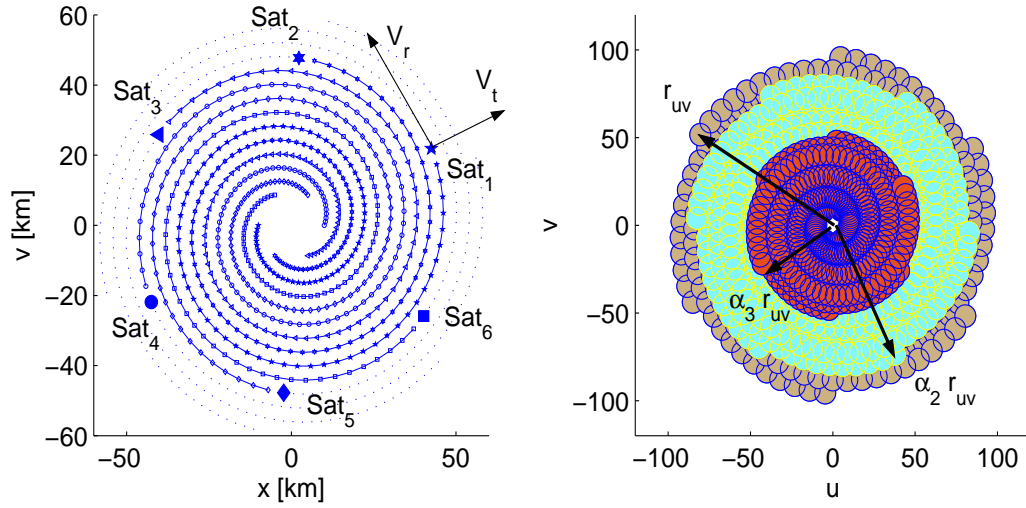
Fig. 9. u-v plane coverage - spiral maneuver

of spiral maneuvers is a convenient choice. Spiral coverage maneuver have been shown to be time optimal [15], they define an optimization problem for the spacecraft trajectories, and allow for rotation of the optical axis to aim at different targets and reorganization in the case of the failure of an individual or a subcollection of spacecraft. The coverage of the u-v plane by a spiral maneuver is shown in Fig. 9.

When defining the problem as a "painting problem" with spiral trajectories the coverage constraints can be described as following: The first coverage constraint is defined by requirement that the total time spent over a given area is greater that the required to have appropriate coverage, that is:

$$\sum_{n=1}^{N_R} \Delta^n(r) \geq \bar{\Delta} \tag{2.72}$$

The maneuvers for the systems studied in this work are considered to be performed by a symmetrical configuration of spacecraft such that a ring structures arises. This configuration of rings is due to the possible combinations of spacecraft pairs for which the mutual coherence can be measured as shown in Fig. 10
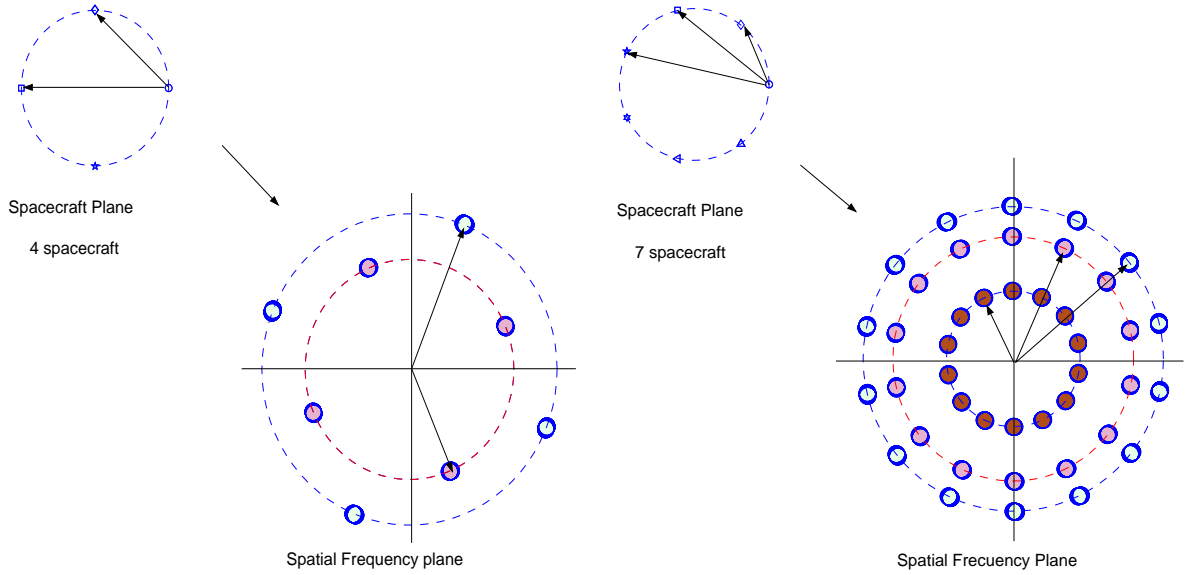
Fig. 10. Ring structure of the spatial frequency coverage of circular arrangement of spacecraft

Following the geometry of the structure it is possible to define $\Delta^{N_R}(r)$ such that such that[5]:

$$2\pi r C dr = CM(\pi\rho^2) \qquad (2.73)$$

$$2\pi r \Delta^{N_R}(r) v_r(r) = M\pi\rho^2 \qquad (2.74)$$

and then:

$$\Delta^{N_R}(r) = \frac{\rho^2 M}{2v_r(r)r} \qquad (2.75)$$

And also from the geometry:

$$\Delta^{N_R-n}(r) = \alpha_n^2 \beta_n \Delta^{N_R}(\alpha_n r) \qquad (2.76)$$

$$\qquad (2.77)$$

Then:

$$\sum_{n=1}^{N_R} \alpha_n^2 \beta_n \frac{\rho^2 M}{2\alpha_n r v_r(\alpha_n r)} \geq \bar{\Delta} \tag{2.78}$$

$$\sum_{n=1}^{N_R} \alpha_n \beta_n \frac{1}{v_r(\alpha_n r)} \geq \frac{2r\bar{\Delta}}{\rho^2 M} \tag{2.79}$$

It is also necessary to guarantee that there are no gaps between turns of the spiral. As the spiral of coverage expands, the coverage disc of one spacecraft must match to the coverage of the next one without leaving any gaps. Then the maximum value of the expansion rate, k, when the size of the discs is constant is given by:

$$k = \frac{dr}{d\theta} \leq \frac{2\rho \beta_{N_R} n_s}{2\pi} \tag{2.80}$$

Notice that for configurations with an odd number of spacecraft, $\beta_{N_R} = 2$, and so this limit is higher, leading to looser spirals.

2. Fuel Optimization Problem for Spiral Maneuvers

Given the coverage constraints and the dynamics of the system, the spiral trajectory fuel optimization problem can be posed as:

$$\min_{\bar{a}_r, \bar{a}_t} \int_0^{R_f} \sqrt{\bar{a}_r^2 + \bar{a}_t^2} dr, \quad subject\ to \tag{2.81}$$

$$\sum_{i}^{N_R} \alpha_i \beta_i \frac{1}{v_r\left(\frac{\alpha_i r}{\alpha_{N_R}}\right)} \geq r\bar{\bar{\Delta}}, \forall r \in [0, R_f], \tag{2.82}$$

$$\frac{r v_r(r)}{v_t(r)} \leq K, \tag{2.83}$$

$$a_r' = f_r(r, v_r, v_t), \tag{2.84}$$

$$a_t' = f_t(r, v_r, v_t), \tag{2.85}$$

$$a_r^2 + a_t^2 \leq A_{max}^2 \tag{2.86}$$

$$\int_0^{R_f} \frac{dr}{v_r(r)} \leq T_{max}. \tag{2.87}$$

where $\bar{\bar{\Delta}} = \frac{2\bar{\Delta}}{\rho^2 M}$. Notice that constraints on 2.82 and 2.83 are coverage constraints, eq. 2.84 and eq. 2.85 are dynamic constraints, eq. 2.86 is the acceleration constraint and eq. 2.87 is the time constraint.

CHAPTER III

QUALITY OF THE IMAGE

In order to calculate the required minimum time of frequency coverage in the maneuvers, it is required to define criteria in the quality of the image, and relate them to the variance of the error in the u-v plane.

It is possible to define different requirements for the quality of the picture. One way is to specify a pixelwise reliability, which limits the error in the value of a every pixel of the image. The other way is to specify the requirement of quality of the picture as a probability of total error of the picture (summation of the squared errors of each pixel).

A. Pixelwise Bound

A requirement of a bound in the error of every point $j \in \tilde{F}_j(i) \geq I_{pth}$ in the image is:

$$Prob\left\{\left|\tilde{F}_j(i(\nu)) - \tilde{F}_j(\hat{i}(\nu))\right| \geq kI_{pth}\right\} \leq p_{max} \tag{3.1}$$

for any $\tilde{F}_j$, where:

$$\tilde{F}_j = v_j^T H^* \, i \tag{3.2}$$

being H^* the inverse Fourier transform, a linear operator that in the discrete case can be defined by the matrix:

$$H^* = h_{i,j}^* = \frac{1}{\sqrt{n}}\omega^{(i-1)(j-1)}, \tag{3.3}$$

$$\omega = e^{\imath 2\pi \Delta r/(\lambda z)}, \tag{3.4}$$

and

$$v_j^T = (0, 0, ..., 1, ..., 0, 0), \tag{3.5}$$

a vector that extracts the value of the jth pixel. kI_{pth} is a maximum value for the error pixelwise, such that every pixel in the actual image with an intensity greater than I_{pth} will have a bounded error. For any point j:

$$
\begin{aligned}
|\tilde{F}_j(i(\nu)) - \tilde{F}_j(\hat{i}(\nu))|^2 &= |v_j^T H^*(i - \hat{i}(\nu))|^2 & (3.6) \\
&= |(i(\nu) - \hat{i}(\nu))^* H v_j v_j^T H^*(i(\nu) - \hat{i}(\nu))|, & (3.7)
\end{aligned}
$$

and:

$$v_j^T H^* = H_j^*, \tag{3.8}$$

$$H v_j = H_j, \tag{3.9}$$

so:

$$
\begin{aligned}
E|\tilde{F}_j(i(\nu)) - \tilde{F}_j(\hat{i}(\nu))|^2 &= |(i(\nu) - \hat{i}(\nu))^* H_j H_j^*(i(\nu) - \hat{i}(\nu))| & (3.10) \\
&= E|H_j^*(i(\nu) - \hat{i}(\nu))(i(\nu) - \hat{i}(\nu))^* H_j| & (3.11) \\
&= H_j^* E|(i(\nu) - \hat{i}(\nu))(i(\nu) - \hat{i}(\nu))^*|H_j & (3.12) \\
&= \sum_1^N h_{ij}^* E|(i(\nu) - \hat{i}(\nu))|^2 h_{ij} & (3.13) \\
&= \sum_1^N h_{ij}^* R_e h_{ij}, & (3.14)
\end{aligned}
$$

R_e being the covariance matrix for the error on the image in the frequency plane, which can be considered diagonal since the measurements in the frequency plane are

uncorrelated. And so

$$E|\tilde{F}_j(i) - \tilde{F}_j(\hat{i})|^2 \quad = \quad \sum_1^N h_{ij}^* h_{ij} E|e(\nu)|^2 \tag{3.15}$$

And because of the symmetry of the operator H, since $h_{ij}^* = (h_{ij})^*$, it follows from Eq.3.3 that $h_{ij}^* h_{ij} = \frac{1}{N}$ and then:

$$E|\tilde{F}_j(i) - \tilde{F}_j(\hat{i})|^2 \quad = \frac{1}{N}||e||_2^2, \tag{3.16}$$

where $||e||_2^2$ is the euclidean norm of $E|e(\nu)|$. This is an exact relation for the value of the variance of the feature.

Since the function $\tilde{F}$ is a linear transformation of $e(\nu)$, and $e(\nu)$ is a gaussian distributed variable, $\tilde{F}(e)$ is a zero mean gaussian distributed variable, with standard deviation given by Eq. 3.16. An exact bound for $||e||_2^2$, such that Eq. 3.1 is satisfied is:

$$||e||_2^2 \leq \sigma_p^2, \tag{3.17}$$

where σ_p is the solution to the equation:

$$p_{max} \quad = \quad 1 - erf\left(\frac{\sqrt{N}kI_{pth}}{\sqrt{2}\sigma_p}\right). \tag{3.18}$$

Correspondingly, this condition is fulfilled if $||e||_\infty^2 = min\{E|e_i|^2\} \leq \frac{||e||_2^2}{N}$, so that Eq. 3.1 is satisfied if

$$\sigma^2[e(\nu)]^2 \leq \frac{1}{Q}, \tag{3.19}$$

where

$$Q = \frac{2(erf^{-1}(1 - p_{max}))^2}{k^2 I_{pth}^2}. \tag{3.20}$$

B.   Chi Squared - Total Error Bound

A bound for the total error in the image can be defined by:

$$Prob\left\{||i(x) - \hat{i}(x)||_2^2 \geq K\right\} \leq p_{max} \tag{3.21}$$

Given Parseval's Theorem[1], the above condition becomes:

$$Prob\{||i(\nu) - \hat{i}(\nu)||_2^2 \geq K\} \leq p_{max} \tag{3.22}$$

Now let's define the complex normal distributed variable:

$$x \quad = \quad \frac{Re(i_j - \hat{i}_j)}{\sqrt{E|Re(i_j - \hat{i}_j)|^2}} + i\frac{Im(i_j - \hat{i}_j)}{\sqrt{E|Im(i_j - \hat{i}_j)|^2}} \sim N(0,1) + iN(0,1) \quad (3.23)$$

And given the acquisition process, the real and imaginary parts are identically distributed random variables. Then:

$$x \quad = \quad \frac{Re(i_j - \hat{i}_j) + iIm(i_j - \hat{i}_j)}{\sqrt{E|Re(i_j - \hat{i}_j)|^2}} \sim N(0,1) + iN(0,1) \tag{3.24}$$

such that:

$$\chi^2 = \sum_{i=0}^{r-1} x^2 \tag{3.25}$$

is a Chi square distributed variable with $r = 2N$. Then, if σ_p is the solution to the equation:

$$1 - \mathscr{G}_r\left(\frac{K}{\sigma_p^2}\right) = p_{max}, \tag{3.26}$$

where,

$$\mathscr{G}_r(y) = \frac{\gamma(r/2, y/2)}{\Gamma(r/2)}, \tag{3.27}$$

and γ, Γ are incomplete and complete gamma functions respectively, Then

$$Prob\left\{\chi^2 \leq \left(\frac{K}{\sigma_p^2}\right)\right\} = p_{max}, \tag{3.28}$$

and

$$||i - \hat{i}||^2 \leq \sigma_p^2 \chi^2, \tag{3.29}$$

$$||i - \hat{i}||^2 \leq \sigma_p^2 \sum_{j=0}^{r-1} \frac{|i_j - \hat{i}_j|^2}{E|Re(i_j - \hat{i}_j)|^2}, \tag{3.30}$$

i.e:

$$\sum_{j=0}^{r-1} \frac{|i_j - \hat{i}_j|^2}{\sigma_p^2} \leq \sum_{j=0}^{r-1} \frac{|i_j - \hat{i}_j|^2}{E|Re(e(\nu_j))|^2}, \tag{3.31}$$

then

$$Prob\{||i - \hat{i}||^2 \geq K\} \leq p_{max} \tag{3.32}$$

The quality condition is then given by Eq.3.31 that describes the hypercone defined by intersection of an hyperellipsoid with the hypersphere given by the left side of the Eq. 3.31. If all the axes of the hyperellipsoid are restricted to be inside the hypersphere, the quality of the image is guaranteed. Then, a solution of Eq. 3.31 that satisfies the error requirement is:

$$\sigma^2[e(\nu)] \leq \frac{1}{Q}, \tag{3.33}$$

where

$$Q = \frac{\mathscr{G}_r^{-1}(1 - p_{max})}{K}. \tag{3.34}$$

Thus, a parameter Q has been defined, that is directly related to the quality of the picture. Fig. 11 shows the same picture for different levels of quality, Q, along with
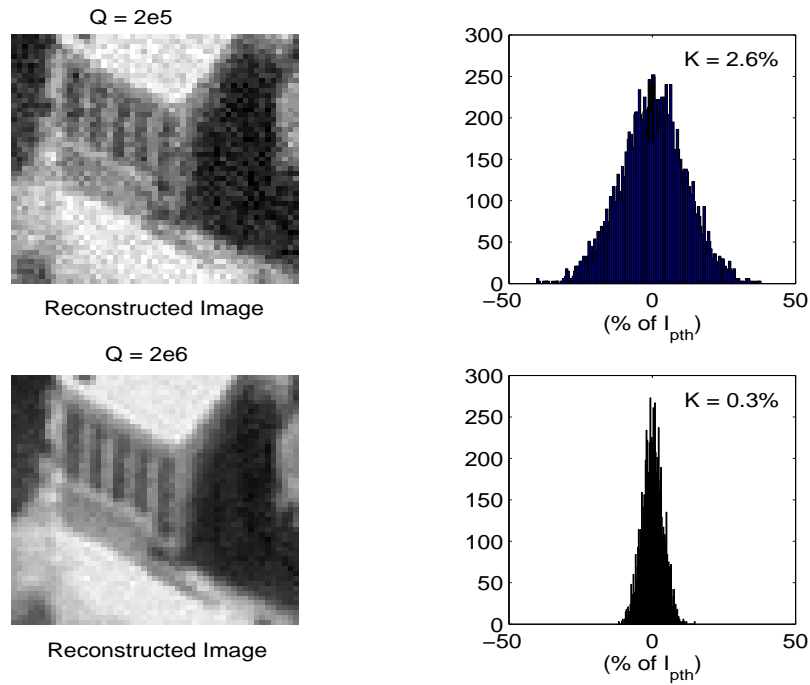
Fig. 11. Quality index of the image. The right side plot displays the error distribution of the pixels and the K value is the total error value K

its total error K and pixel wise error distribution k.

A relationship between, k (the quality), p_{max} (the probability of getting an error worse than that), and the trajectories of the spacecraft has been thus defined. Fig. 12 shows Q as a function of the Error Probability for different k (the pixelwise quality) for different probabilities, and Fig. 13a shows Q as a function of K (the total error quality) for different values of p_{max} (notice that it is basically constant). Fig. 13b shows the quality index Q as the value of K is increased.

Fig. 12. Pixelwise quality vs error probability for different k

Fig. 13. a. Total quality vs error probability for different K . b. Total quality vs K for probability = 50%

CHAPTER IV

DEEP SPACE SOLUTION: THE PANTOGRAPHIC PROBLEM

In this chapter a solution to the Optimization process posed in Eqs.(2.81)-(2.87) under deep space dynamics, i.e. double integrator, non-perturbed dynamics is described.
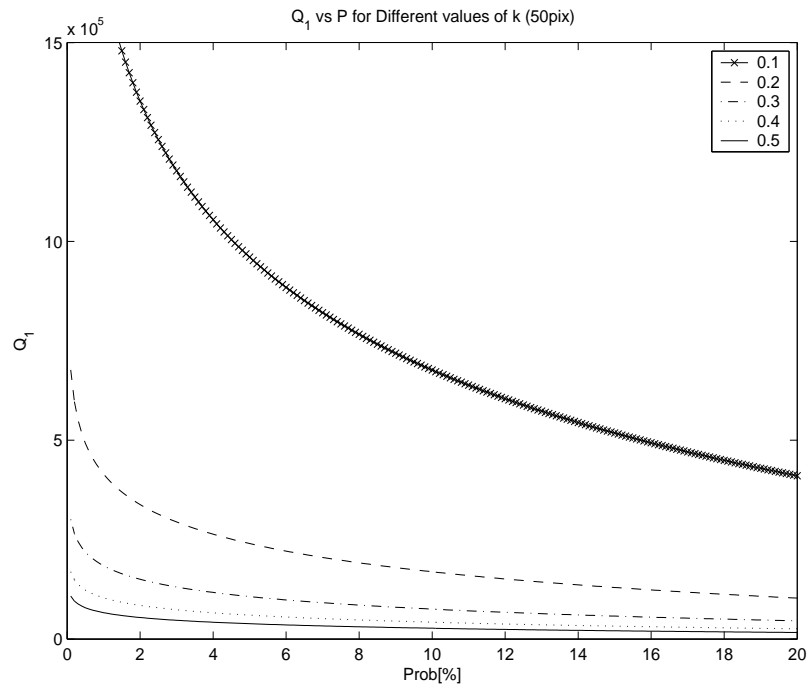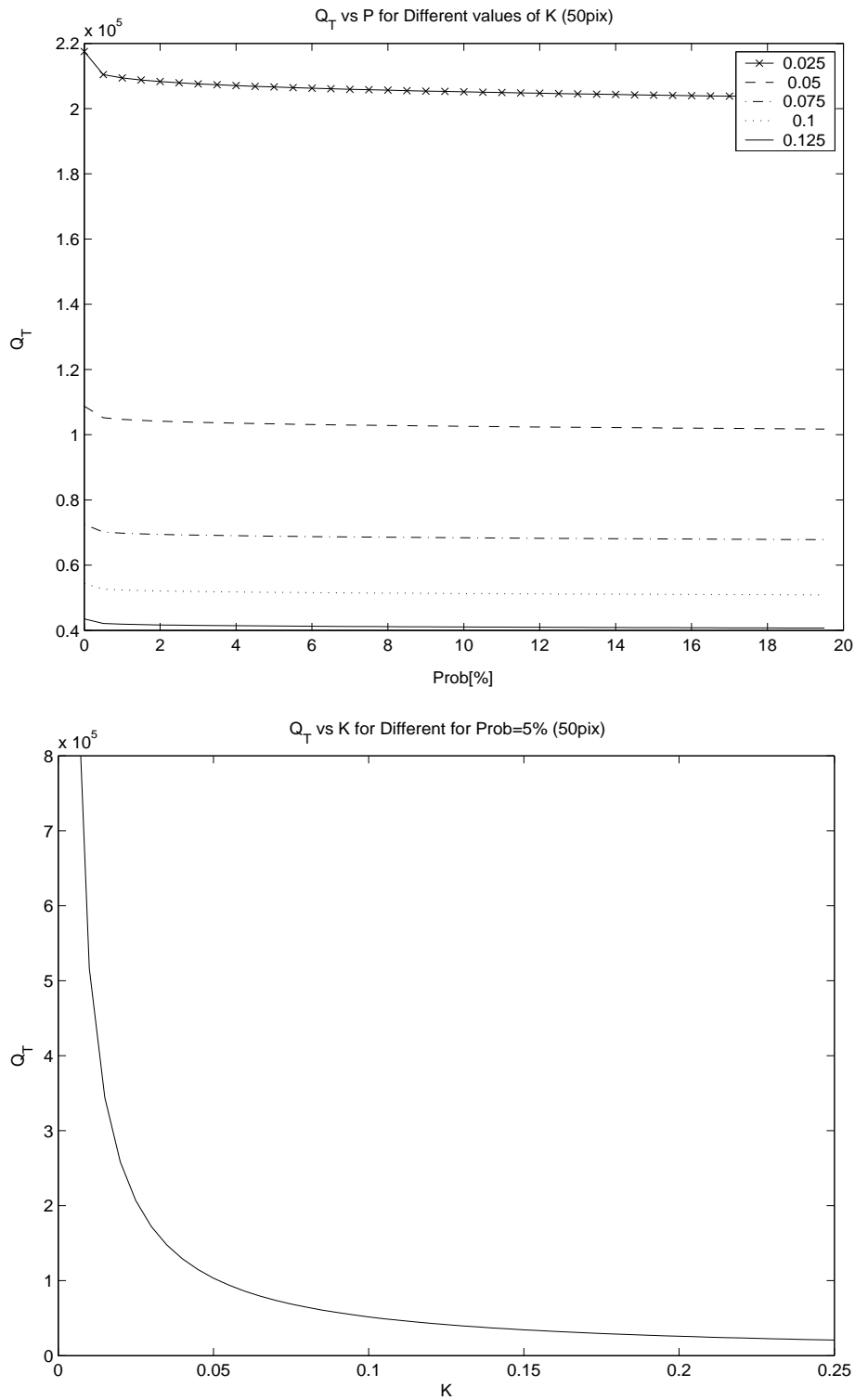
For a satellite describing a spiral in deep space, the dynamic equations can be written in the form [16]:

$$\bar{a}_r(r) = \frac{a_r(r)}{v_r(r)} = \left(\frac{dv_r}{dr} - \frac{v_t}{k} \right), \tag{4.1}$$

$$\bar{a}_t(r) = \frac{a_t(r)}{v_r(r)} = \left(\frac{dv_t}{dr} + \frac{v_r}{k} \right). \tag{4.2}$$

The optimization problem under these conditions is solved, for the constrained case and for large times of maneuver (i.e unconstrained or weakly constrained cases) and 4 satellites. The numerical solution was obtained for 2 cases. First, a sub-optimal solution was obtained using k constant, with v_r as the optimization variable. In the second approach, an optimal solution was obtained with both v_r and v_t both as optimization variables.

Solutions were found for different values of number of intervals and different mission quality constraint. It was found in all the cases that the optimal solution corresponds to the loosest spiral, i.e the spiral with the maximum possible spiraling rate.

Since the cost function is monotonically decreasing for any $k \geq 0$ it is expected that the value of k, which minimizes J, is attained at the constraint boundary; numerical solutions to the problem seem to corroborate these observations. Fig. 14a and 14b compare the solutions to the sub-optimal problem with fixed radial rate (i.e. k fixed) and the true optimal (i.e. v_r and v_t as optimization variables) problem. The

40
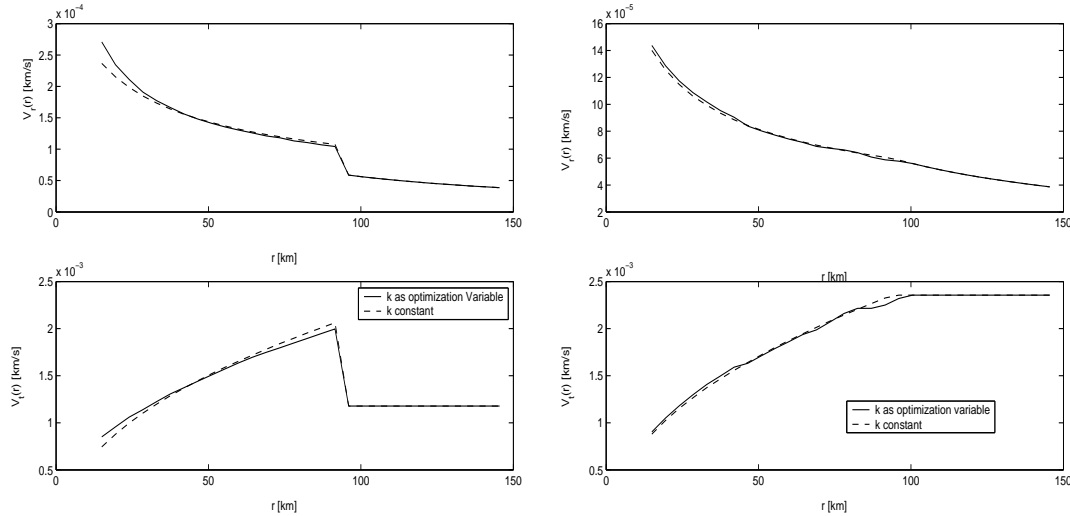
Fig. 14. Comparison of solutions for the fixed expansion rate and the optimal expansion rate cases for: a. Active constraints case (left), and b. Not active constraints(right)

solution on the left shows the velocities of a trajectory for a case where constraints are active, it clearly displays the discontinuity of the solution caused by the character of the constraint which acts only on part of the total radial distance. The plot on the right side shows the solution obtained for a case where the time of maneuver is higher and the constraints are not active. In both cases the value of k lays at the constraint boundary. The small difference in the solution may be attributed to the discretization of the problem since in the optimal expansion rate case the solution converges to a value of k for every r, that is close to the limit value up to the tolerance of the solving algorithm.

Hence, in accordance with the observations above, the following approximation is made:

For a fixed time, the optimal fuel maneuver is obtained when k is the maximum value allowed by the radial expansion limit, and the problem is thus reduced to the MFKD problem.

The dynamics of the system in deep space can then be written as:

$$\bar{a}_r(r) = \frac{a_r(r)}{v_r(r)} = \left(\frac{dv_r}{dr} - \frac{v_t}{k} \right), \tag{4.3}$$

$$\bar{a}_t(r) = \frac{a_t(r)}{v_r(r)} = \left(\frac{r}{k} \frac{dv_r}{dr} + 2\frac{v_r}{k} \right). \tag{4.4}$$

and, for the cases under consideration, since the rate of change of velocity with respect to the radial distance is small, the contribution of $\frac{dv_r}{dr}$ can be assumed to be negligible. Figure 15 shows the small difference in the calculation of the acceleration when including the term. In the total cost function the contributions of these terms can be neglected and under the above approximations, Eq.(2.81) can be written as:

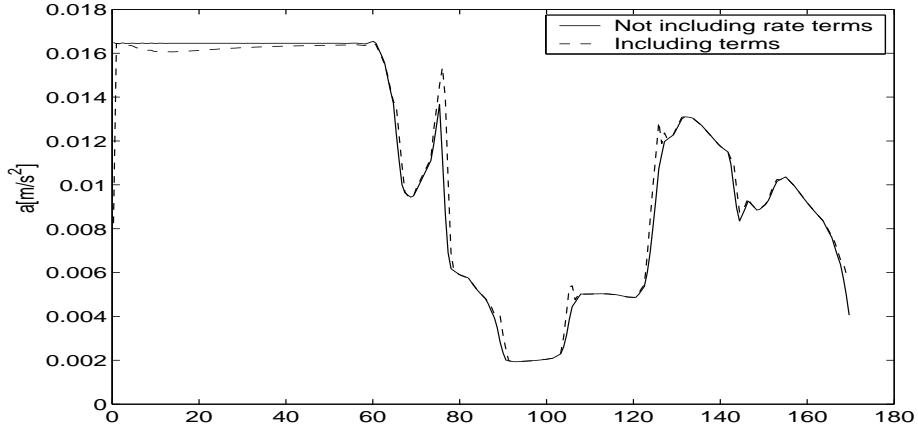$$J = \int_0^{R_{max}} \frac{v_r(r)}{k^2} \sqrt{r^2 + 4k^2} dr \tag{4.5}$$

Fig. 15. Small influence of rate terms in total cost

A. Solution for the Constrained Fuel Optimal Problem with n Spacecraft

In order to obtain a solution to the minimum fuel spiral maneuver problem, the problem is discretized as follows:

$$\Phi_i = \Phi(r_i) \quad i = 1, ... n_s \tag{4.6}$$

$$\Phi(r) = \frac{1}{v_r(\alpha_m r)} \tag{4.7}$$

where m is the number of rings in the configuration, namely $m = 2$ for 4 and 5 spacecrafts, $m = 3$ for 6 and 7, and so on. The constants α_i (see sec. 4) are proportionality constants for each ring, (e.g. $\alpha_2 = \sqrt{2}$ for 4 spacecraft) and α_M is the value for the smallest ring in a given configuration.

Following this discretization, the constraints can be written as linear inequality constraints Eqs.() and (), The constraints become:

1. FPC Constraint

The Full Paint Coverage constraint, Eq. 2.82, can be written for the general case with n spacecraft and m rings as:

$$\sum_i^{N_R} \alpha_i \beta_i \frac{1}{v_r(\frac{\alpha_i r}{\alpha_{N_R}})} \geq r\bar{\bar{\Delta}}, \forall r \in [0, R_f] \tag{4.8}$$

where $\bar{\bar{\Delta}}$ is a constant proportional to the image quality. Given the optimization variable the constraints can be written into the following pantographic constraint (pantographic constraints are equivalent to time delayed constraints):

$$\sum_i^{N_R} \alpha_i \beta_i \Phi(\alpha_i r) \geq r\bar{\bar{\Delta}}, \quad r \in (R_{min}, R_{max}). \tag{4.9}$$

When the problem is discretized, the FPC pantographic constraints can be written as following linear constraint:

$$\Gamma \cdot \underline{\Phi}(r) \geq \underline{r}\bar{\bar{\Delta}}, \tag{4.10}$$

where Γ is a matrix given by:

$$\Gamma = \sum_1^m \alpha_i \beta_i \mathscr{W}_{(\alpha_i/\alpha_m)}. \tag{4.11}$$

Here $\alpha_1 = 1$, $\beta_1 = 1$, m is the number of rings, and the matrix $\mathscr{W}_\alpha$ is the approximation in discrete space of the operator:

$$\mathscr{F}_\alpha(\Phi(r)) = \Phi(\alpha r), \tag{4.12}$$

which has the form:

$$\Phi(\alpha r) = \mathscr{W}_\alpha \cdot \Phi(r) \tag{4.13}$$

$$= \begin{bmatrix} 1 & 0 & \dots & 0 & 0 & \dots & 0 & 0 \\ 0 & \dots & 0 & p & 1-p & 0 & \dots & 0 \\ & & & \dots & & & & \\ 0 & \dots & 0 & 0 & 0 & 0 & 0 & 1 \\ 0 & 0 & 0 & 0 & 0 & 0 & 0 & 0 \\ & & & \dots & & & & \\ 0 & 0 & 0 & 0 & 0 & 0 & 0 & 0 \end{bmatrix} \begin{bmatrix} \Phi(r_i) \\ \Phi(r_{i+1}) \\ . \\ . \\ . \\ \Phi(r_{n_s-1}) \\ \Phi(r_{n_s}) \end{bmatrix}, \tag{4.14}$$

where p is a proportionality constant that calculates the value of Φ at the point αr, as the linear interpolant of $\Phi(r_{i-1})$ and $\Phi(r_i)$. As a particular case, $\mathscr{W}_1$ is the identity matrix.

The importance of defining the discretized optimization variable as done in 4.7, i.e. the inverse of the velocity of the smallest ring, is illustrated in Fig. 16.

A pantographic equation:
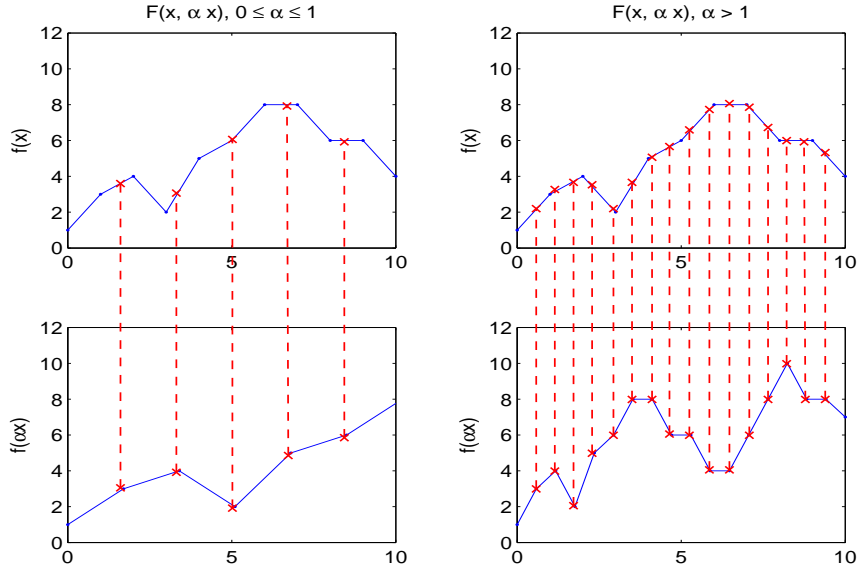
Fig. 16. Pantographic constraints

$$f(x_i, \alpha x_i) \leq K \quad \forall x_o \leq x_i \leq x_f \tag{4.15}$$

when $\alpha > 1$, does not constraint the function $f(x)$ at every point inside its range. In such a case the number of constraints is less than discrete points of the variable. However, when $0 < \alpha \leq 1$, the variable is constrained at every point inside its validity range, and the discrete optimization can be properly posed.

2. Time Constraint

The time constraint is given by the integral in Eq.(36):

$$\int_0^{R_f} \frac{dr}{v_r(r)} \leq T_{max}, \tag{4.16}$$

which after discretization, using a zero hold integration scheme, can be written as the vector product:

$$V \cdot \Phi \leq T_{max} \qquad (4.17)$$

where $V = \alpha_M \delta r [0.5 \ 1 \ 1...1 \ 0.5]$, and δr is the distance between two contiguous discrete radial points.

Then, an optimization for the trajectories subject to deep space dynamics can be obtained for the discretized optimization variable $\Phi(r)$ defined in Eq. 4.7:

$$Min \ J = \sum_{i=1}^{N} \frac{1}{\Phi_i} \cdot \frac{\sqrt{r_i^2 + 4k_i^2}}{k_i^2}, \quad subject \ to: \qquad (4.18)$$

$$\Gamma \cdot \Phi \geq r\Delta, \qquad (4.19)$$

$$\alpha_N \bar{1}^T \Phi = \alpha_N ||\Phi|| \leq T_{max}, \qquad (4.20)$$

$$\Phi_i^2 \geq \frac{\sqrt{r_i^2 + 4k_i^2}}{k_i^2 A_{max}} \qquad (4.21)$$

B.   The Optimal Solution

The necessary condition of the solution to the discretized problem in Eq. 4.21 can be obtained when defining the Hamiltonian:

$$H = C^T \cdot \frac{1}{\Phi} - \lambda^T (\Gamma \Phi - r\Delta) - \mu(T_{max} - \alpha_N \bar{1}^T \Phi) + \eta^T (A_{max} \bar{1} - diag[C] \frac{1}{\Phi^2})$$

$$(4.22)$$

Here:

$$C_i = \frac{\sqrt{r_i^2 + 4k_i^2}}{k_i^2}, \qquad (4.23)$$

λ and η vectors and the scalar μ are Lagrange multiplier for the constraints, and $diag[x]$ is a square diagonal matrix with the elements in the diagonal being the element in the vector x.

These multipliers, given Poyntriagin's principle (and a small rearranging), must satisfy:

$$\lambda_i \begin{cases} = 0 & if \quad \Gamma_i \Phi \leq r_i \Delta \\ > 0 & if \quad otherwise \end{cases} \tag{4.24}$$

$$\eta_i \begin{cases} = 0 & if \quad \Phi_i \leq \sqrt{\frac{C_i}{A_{max}}} \\ > 0 & if \quad otherwise \end{cases} \tag{4.25}$$

$$\mu \begin{cases} = 0 & if \quad ||\Phi||_1 \geq T_{max} \\ > 0 & if \quad otherwise \end{cases} \tag{4.26}$$

Being $|| \cdot ||_1$, the one-norm of a vector.

The Lagrange Necessary conditions for optimality give us:

$$0 = \nabla_\Phi H \tag{4.27}$$

$$= -diag\left[\frac{1}{\Phi^2}\right] C - \Gamma^T \lambda + \alpha_N \bar{1} - diag[C] diag\left[\frac{2}{\Phi^3}\right] \eta \tag{4.28}$$

And thus we have a system of 2N+M+1 equations, and 2N+M+1 unknowns that can be solved numerically.

Concerning the convexity of this optimization space notice the following facts:

- We defined our system to be confined to only the positive subspace.

- Therefore, the cost function is a weighted summation of convex hyperbolas, therefore, the Cost function is convex.

- The time constraint is a plane that define the one norm

- The acceleration constraints are hypercubes limiting the minimum value of Φ

- The FPC Constraint is a simplex surface conformed by linear combinations of the optimization variables

The previous remarks are explained in the diagram in Fig. 17, where the problem is shown for $\Re^2$.
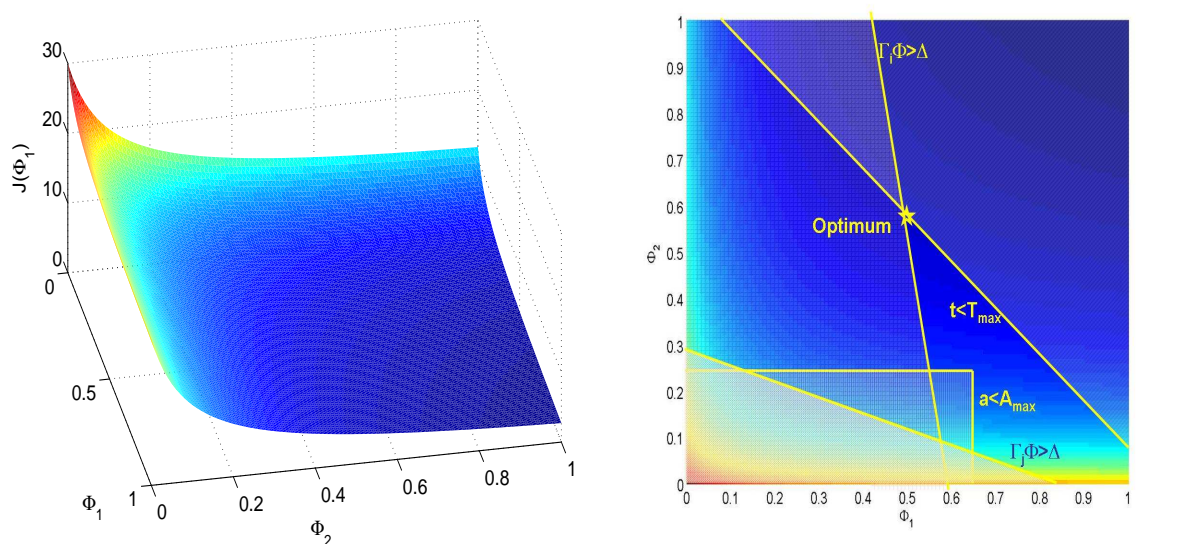

Fig. 17. Convexity of the optimization problem

C. Deep Space Solutions for Planet Imaging

Given the convexity of the optimization space, as seen above, a solution to the Non-Linear Programming problem can be formed using a Sequential Quadratic Programing algorithm like `fmincon` or `SNOPT` in MATLAB.

Minimum fuel cost trajectories for MSIIS comprising 4 to 14 spacecraft were

calculated using the method described above for different maximum times of maneuver. The parameters used correspond to imaging mission to detect the bandedness of a Jupiter sized planet at a distance of 25 light years, provided in previous reference.[15].50x50 pixel images of the planet are considered. These parameters are:

- R = 100 kilometers,

- $\rho = 0.02$,

- C = 2.5,

- B = 2×10^{-4},

- $\mu = 1000$ photons/s,

are used to calculate $\bar{\bar{\Delta}}$ and run the optimization algorithm.

The results are displayed in Table I. From them, insight into the cost of MSIIS missions can be obtained, the order of magnitude of the required accelerations, and the general behavior of a maneuver covering the frequency plane. The results show that as the number of satellites is increased, a shorter time of maneuver is feasible, and the total fuel cost of an imaging maneuver is reduced. The maximum thrust required (T_{MAX}) is calculated per 100 kg mass of the constituent spacecraft

Some plots of the obtained solutions are shown in Figs. 18-21. The plots show the time history of the acceleration and the values of the corresponding velocities. The lower plot in these figures describes the fulfillment of the constraint, displaying the ratio of the time of light collection with respect to its requirement. The space trajectories of each of the maneuvers only depend on the value of k (fixed for a given number of spacecraft). Figure 9 shows the maneuver for 6 spacecraft. In Fig. 18 the results for a non-constrained case are shown, i.e., a case in which the FPC are not active. The time of maneuver in this case is high. As the time of maneuver is

Table I. Cost for different number of satellite (n_s) and different time of maneuver (time)

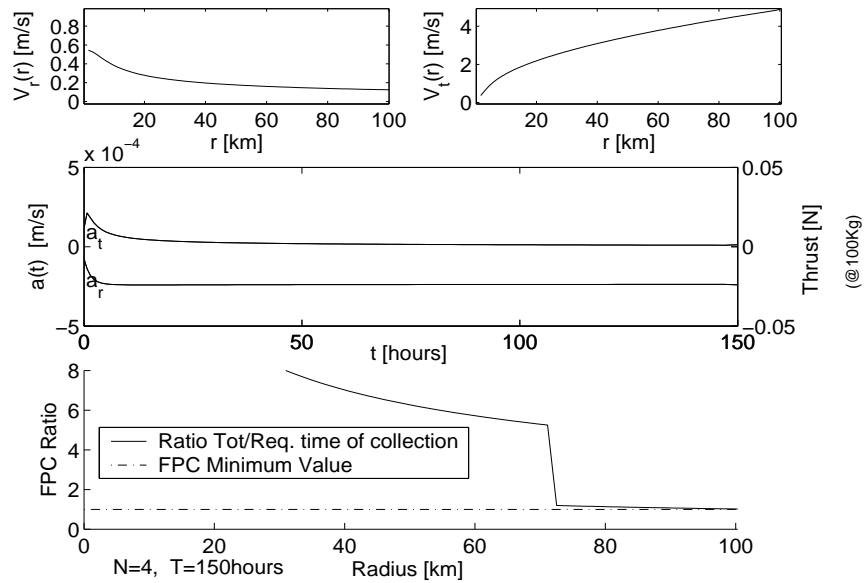| n_s	time	ΔV	T_{MAX}
	[hours]	[m/s]	[mN]/100 Kg
4	80	339	344
4	60	947	438
4	46	1337	2367
5	80	104	3574
6	60	207	487
6	30	1138	2846
7	80	27	19
7	30	175	812
8	80	209	69
8	30	556	495
8	24	696	774
8	20	836	1128
9	80	16	28
9	24	171	826
10	80	135	45
10	24	510	453
10	12	971	7463
11	30	82	75
11	24	104	139
12	24	361	363
12	12	770	1749
13	24	91	104
13	18	122	189

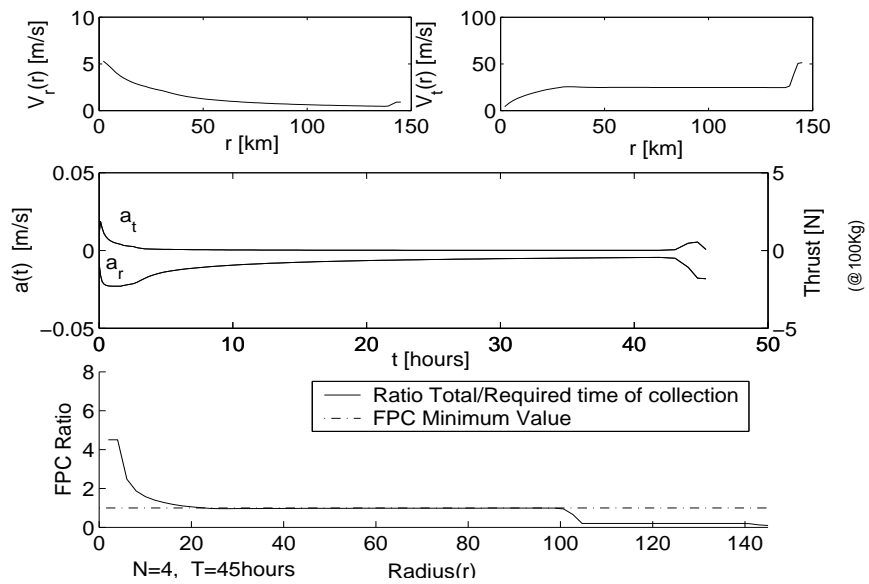Fig. 18. State history for 4 spacecraft, 150 hours FPC not active

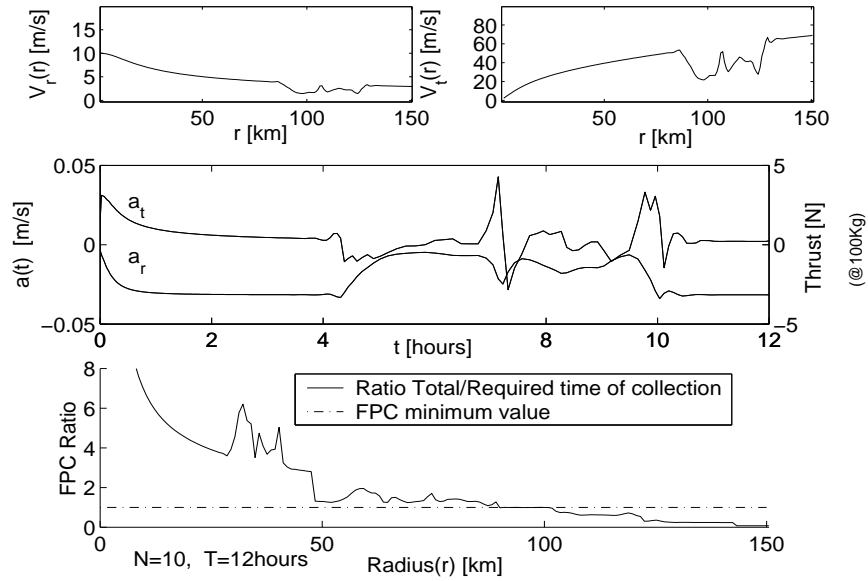Fig. 19. State history for 4 spacecraft, 45 hour maneuver with active constraints

Fig. 20. State history for 10 spacecraft, 12 hour maneuver with active constraints
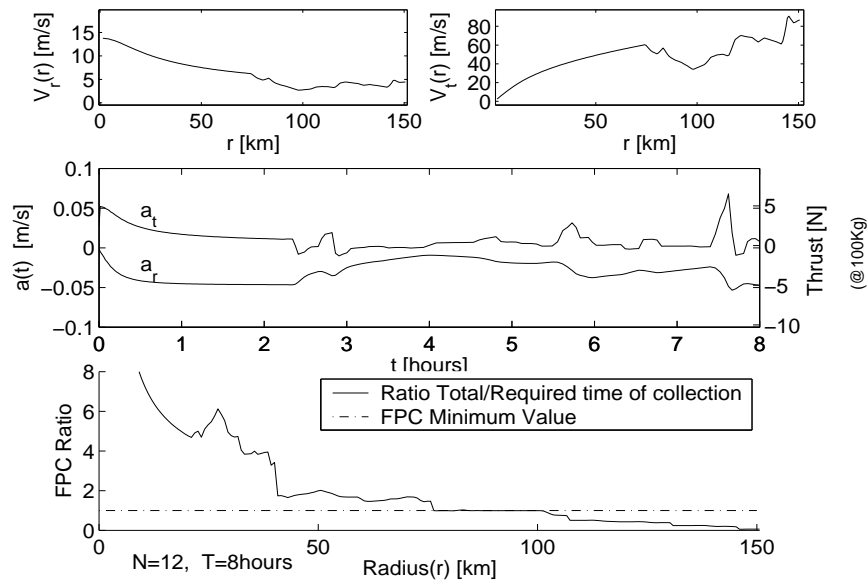
Fig. 21. State history for 12 spacecraft, 8 hour maneuver with active constraints

reduced to the minimum feasible time, the optimal velocities increase and the FPC becomes active. Figs. 19, 20 and 21 show the solutions obtained for constrained low-time cases. In Fig. 19, a near-minimum time maneuver of 45 hours is shown for a 10 spacecraft system, and in Figs. 20 and 21, maneuvers are shown for 10 spacecraft in 12 hours and for 12 satellites in 8 hours respectively.

From the above mentioned results the actual cost of the imaging maneuver is calculated and the maximum acceleration required for such high resolution imaging missions. Maneuvers achievable in reasonable times are found to require reasonable fuel to total mass ratio. As an example, for a hundred of such maneuvers, with $I_{sp} = 7000\ s$, using 8 spacecraft in 24 hour missions, a spacecraft would require a ratio of fuel mass to total mass of [20]:

$$\frac{M_f}{M_t} = 1 - e^{-\Delta V/I \cdot g} = 0.63 \tag{4.29}$$

Figure 22 shows the results for the fuel to total mass ratio for one hundred
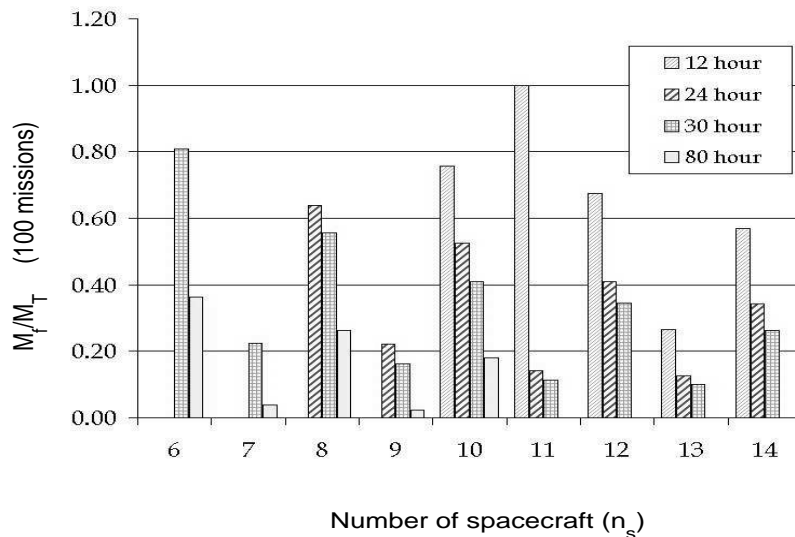
Fig. 22. Mf/Mt ratio for different number of spacecraft and different times of maneuver

maneuvers, as a function of the number of spacecraft and for different times of maneuver. The particular imaging mission considered requires a very high level of light collection due to the feature selected as the criterion for classification[6]. Other missions would require much lower levels which would lead to less stringent time and fuel requirements.

Maneuvers lasting 24 hours comprising 13 spacecraft, require a maximum thrust of 100 mN (per 100 Kg of mass) and a total ΔV of the order of 0.09 km/s. 24-hour maneuvers with fewer than 9 satellites show a maximum required thrust of the order of 1 N (per 100 kg of total mass). Such high impulses are however practically infeasible using current electrical propulsion technologies due to the power supply constraints.

CHAPTER V

NEAR-MINIMUM FUEL MANEUVERS IN NEAR EARTH-ORBIT

In this chapter the design of multi-spacecraft interferometric imaging systems (MSIIS) located in a near earth orbit is studied.

In the previous chapters the dynamics of the spacecraft have been related to the Modulation Transfer Function (MTF) of the optical system and a time/fuel optimal problems have been posed. In this section, a solution algorithm is proposed to calculate near-minimum fuel trajectories in near earth orbit. It is intended to find solutions to the optimization problem Eqs.(2.81)-(2.87) subject to Clohessy-Wiltshire (CW) dynamical equations.

The problem was solved for deep space dynamics in the previous chapter, but the symmetry utilized to solve the problem for that case is lost for the case of CW dynamics [21]:

$$\ddot{x} - 2n\dot{y} - 3n^2x \;=\; u_x \tag{5.1}$$

$$\ddot{y} + 2n\dot{x} \;=\; u_y \tag{5.2}$$

$$\ddot{z} + n^2z \;=\; u_z \tag{5.3}$$

and therefore, the cost function J, not only depends on the radial and tangential components of the velocities in the spiral but is also dependent on the trajectory of each individual. Solving this optimization problem requires the solution of the trajectories of the spacecraft in three-dimensional space subject to asymmetric dynamics. When the problem is posed for formations in near-earth orbit the symmetry and other desirable features of the optimization problem in the case of deep space, such as convexity, disappear, and the structure of the problem does not allow for the design of a computationally efficient optimization method for the exact problem.

A near minimum fuel solution of the problem is proposed assuming that the total cost of the maneuver for n spacecraft is optimized by dividing the problem into two subproblems: First, the spacecraft maneuvers are optimized assuming deep space dynamics , i.e. non-perturbed double integrator. Next, the resulting trajectories are tracked under C-W dynamics using a Linear Quadratic Regulator optimal control.

In the previous chapter, the process where the optimization problem is converted to a Non Linear System that can be solved by a SQP algorithm for deep space dynamics has been considered.

Using that algorithm, the first stage of the problem is solved for the parameters of the imaging system and the obtained trajectories are an input for an LQR tracker controller.

For the LQR problem, the dynamical system is:

$$
\begin{bmatrix} \dot{x} \\ \dot{y} \\ \dot{z} \\ \ddot{x} \\ \ddot{y} \\ \ddot{z} \end{bmatrix} = \begin{bmatrix} 0 & 0 & 0 & 1 & 0 & 0 \\ 0 & 0 & 0 & 0 & 1 & 0 \\ 0 & 0 & 0 & 0 & 0 & 1 \\ 3n^2 & 0 & 0 & 2n & 0 & 0 \\ 0 & -2n & 0 & 0 & 0 & 0 \\ 0 & 0 & -n^2 & 0 & 0 & 0 \end{bmatrix} \begin{bmatrix} x \\ y \\ z \\ \dot{x} \\ \dot{y} \\ \dot{z} \end{bmatrix} + \begin{bmatrix} 0 & 0 & 0 \\ 0 & 0 & 0 \\ 0 & 0 & 0 \\ 1 & 0 & 0 \\ 0 & 1 & 0 \\ 0 & 0 & 1 \end{bmatrix} \begin{bmatrix} u_x \\ u_y \\ u_z \end{bmatrix},
$$

$$(5.4)$$

and the trajectory to be tracked is:

$$
\mathbf{r}(t) = \begin{bmatrix} y_t(t) \\ z_t(t) \\ \dot{y}_t(t) \\ \dot{z}_t(t) \end{bmatrix} = \begin{bmatrix} r\cos(\theta) \\ r\sin(\theta) \\ k\omega(\cos(\theta) - kr\sin(\theta)) \\ k\omega(\sin(\theta) + kr\cos(\theta)) \end{bmatrix}
$$

$$(5.5)$$

where k is the expansion rate of the spiral and ω, r, and θ are defined from the solution of the NLP solution in the first stage.

Then, the cost function of the LQR optimal problem is [22]:

$$J = \frac{1}{2}(Cx(T) - r(T))^T \mathbb{P}(Cx(T) - r(T)) + \frac{1}{2}\int_t o^T(Cx - r)^T \mathbb{Q}(Cx - r) + u^T \mathbb{R}u\,dt \quad (5.6)$$

with,

$$C = \begin{bmatrix} 0 & 1 & 0 & 0 & 0 & 0 \\ 0 & 0 & 1 & 0 & 0 & 0 \\ 0 & 0 & 0 & 0 & 1 & 0 \\ 0 & 0 & 0 & 0 & 0 & 1 \end{bmatrix} \quad (5.7)$$

Note, that the x direction (optical axis direction) is free, and the spiral is projected on the y-z directions of the local vertical, local horizontal (LVLH) coordinate system.

Then, the controller

$$u(t) = -R^{-1}B^T S(t)x + R^{-1}B^T v \quad (5.8)$$

is an optimal control for the desired trajectory, with:

$$-\dot{S} = A^T S + SA - SBR^{-1}B^T S + C^T QC, \quad (5.9)$$

$$-\dot{v} = (A - BK)^T v + CQ\mathbf{r}(t). \quad (5.10)$$

This algorithm accounts for the orbital dynamics of small displacements about a near circular orbit and the requirements on acceleration and required thrust, describing the imaging spirals in the desired plane.

Fig. 23 shows the results for one of these maneuvers. The trajectory shown is the trajectory of 1 of the spacecraft, of a 13 spacecraft maneuver, projected in the
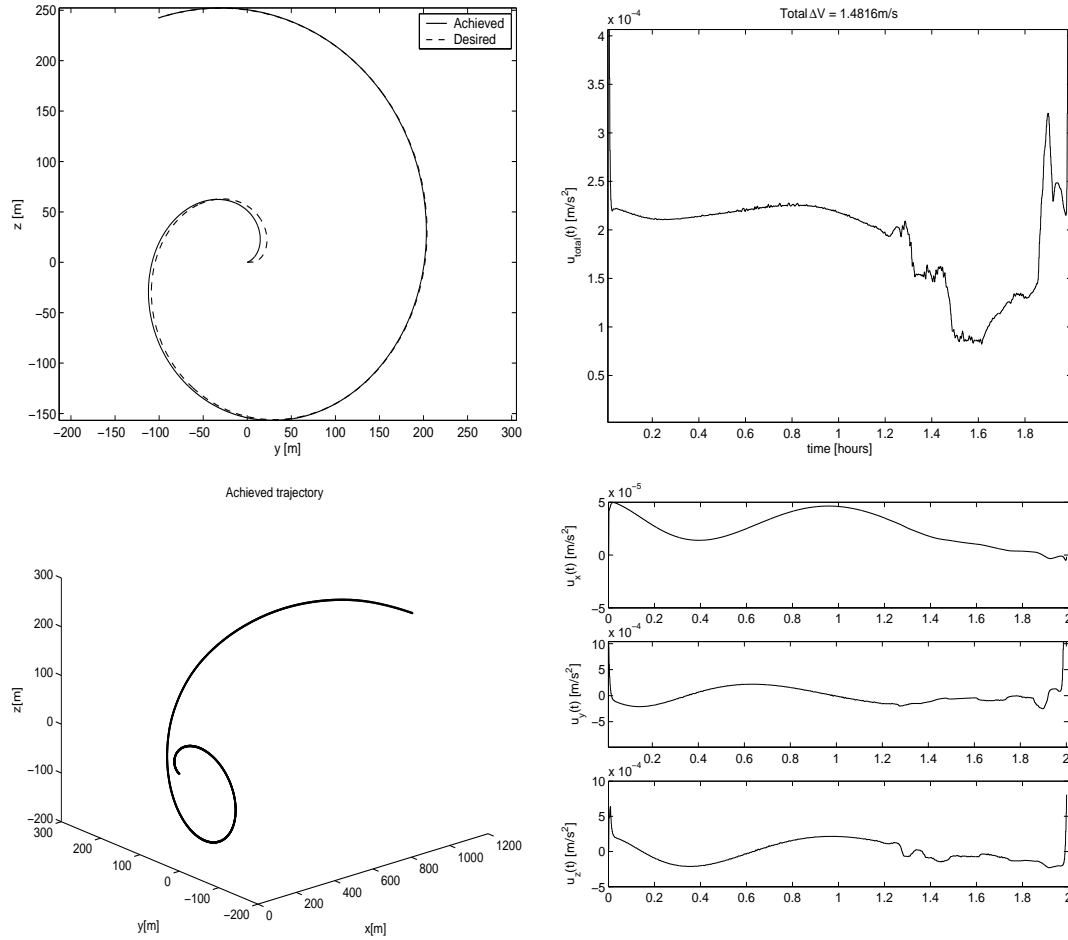
Fig. 23. 11 spacecraft 2 hour maneuver, resolution on target = 1 m

the LHLV plane.

Fig. 24 displays the trajectories of 5 out of 13 spacecraft in a 2 hour maneuver, and the three-dimensional paths described. These trajectories obviously do not intersect, and although they are not confined to a plane, they do project the optimal trajectories in the perpendicular plane to the optical axis.
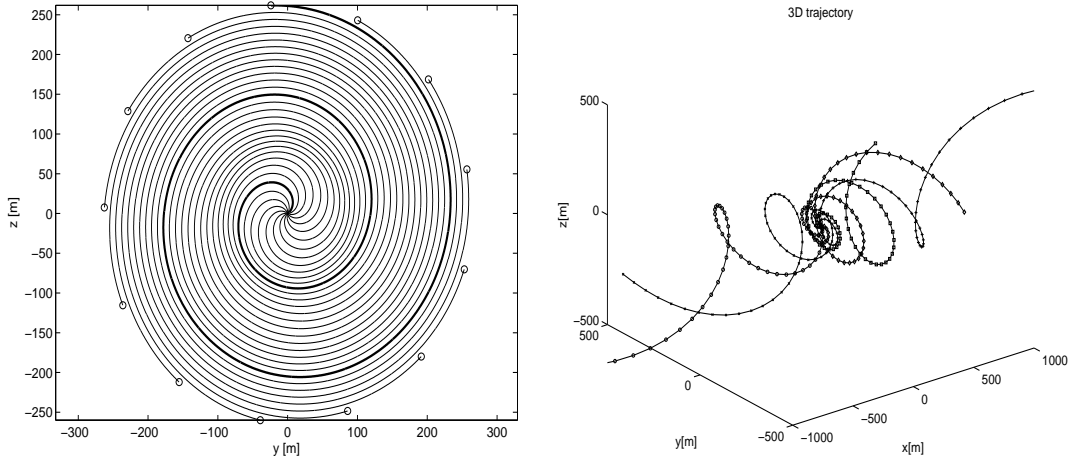
Fig. 24. 13 spacecraft 3 hour maneuver, $100 \times 100pix$. Left: Projected path in the yz plane of the 13 spacecraft. Right: 3D trajectories of 5 of the spacecraft in the LHLV reference frame

A.   Results for the Algorithm - Application to a Mid-IR Imaging System in GEO Orbit

In this section, the results for the solutions of the optimization problem posed above are described, and the behavior for selected parameters and different configurations are displayed, in order to describe the relation between the fuel consumption and the quality of the reconstructed images.[2]

The diameter of the maneuver is defined by the desired resolution of the image, by the position of the first zero in the interferometric pattern of Airy disc, that is approximately[1]:

$$D = 1.22\frac{\lambda \bar{z}}{\delta},\tag{5.11}$$

where δ is the resolution of the picture. If the design is calculated for $\lambda = 10\mu m$ and an approximate resolution of 1 m in the target, the diameter of the optical aperture has to be about 500m.

The minimum size of the collecting telescopes required to acquire the light from the prescribed area of the target is given by the same criteria[1], and is inversely proportional to the resolution d_{pix} and the number of pixels in the picture, n_{pix}:

$$D_{mtel} = 1.22 \frac{\lambda \bar{z}}{n_{pix} d_{pix}}. \tag{5.12}$$

The rate of arrival of photons for imaging an thermally radiating object on earth can be calculated as [23]:

$$\mu_{tot} = \frac{2c}{\lambda^4 (e^{hc/\lambda kT} - 1)} \frac{\eta \xi (\Delta \lambda) 2 A_{tel} (d_{pix} n_{pix})^2}{\bar{z}^2} \; [ph/s], \tag{5.13}$$

where ξ is the emissivity coefficient of the radiating body, that can be as low as 0.1, η is the absorption coefficient of the atmosphere at the given wavelength, and A_{tel} is the area of the telescopes. The bandwidth $\Delta \lambda$ is a parameter limited by the desired resolution and the measuring system. In the case of heterodyne interferometry, it is of the order of 2nm[3], and can be greater in the case of direct interferometric methods.

The factor $\bar{\Delta}$ in Eq.(7), in the optimization problem previously mentioned, can be expressed for the direct detection as(Ref. Eq.(20)):

$$\bar{\Delta} = \left(1 + \frac{1 - \epsilon}{\tau_{opt} n_s (e^{h\nu/kT_{opt}} - 1)}\right) \frac{(M-1)^2 Q_d}{\tau_{opt} \varsigma \mu_{tot}}, \tag{5.14}$$

such that in the case of the thermal source, the term $\bar{\bar{\Delta}}$ in the spiral trajectory optimization (Eq.12) is:

$$\bar{\bar{\Delta}} = \left(1 + \frac{1 - \epsilon}{\tau_{opt} n_s (e^{h\nu/kT_{opt}} - 1)}\right) \frac{(M-1)^2 \lambda^4 \bar{z} (e^{hc/\lambda kT} - 1)}{2 \tau_{opt} \varsigma \eta \xi c M (\Delta \lambda) A_{tel} d_{pix}^2} Q_d. \tag{5.15}$$

And replacing the minimum size of the telescope:

$$\bar{\bar{\Delta}} = \left(1 + \frac{1 - \epsilon}{\tau_{opt} n_s (e^{h\nu/kT_{opt}} - 1)}\right) \frac{2 n_{pix}^2 (M-1)^2 \lambda^2 (e^{hc/\lambda kT} - 1)}{\varsigma \eta \xi c M (\Delta \lambda) (1.5\pi)} Q_d. \tag{5.16}$$

Similarly, for heterodyne detection, from Eq.(22) $\bar{\Delta}$ can be written as:

$$\bar{\Delta} = \left(1 + \frac{1}{n_s} + \frac{1 - \epsilon}{n_s(e^{h\nu/kT_{opt}} - 1)} \right) \frac{Q_h}{\mu_{tot}}, \tag{5.17}$$

such that in this case

$$\bar{\bar{\Delta}} = \left(1 + \frac{1}{n_s} + \frac{1 - \epsilon}{n_s(e^{h\nu/kT_{opt}} - 1)} \right) \frac{2n_{pix}^2 \lambda^2 (e^{hc/\lambda kT} - 1)}{cM\eta\xi(\Delta\lambda)1.5\pi} Q_h, \tag{5.18}$$

where Q is the image Quality factor mentioned in the previous section, n_{pix} is the number of pixels in the image, and M is the number of spacecraft.

Simulations and calculation of fuel consumption for different maneuver were performed. Figs. 23 and 24 show the features of these type of maneuvers. In Fig. 23, the plots show the values for the accelerations in all the three axes, as well as the tracking of the trajectories by the inner loop controller. Notice that the level of acceleration in the x direction is orders of magnitude smaller that in the other directions. Notice as well that the major discrepancies are at the beginning of the tracking. This behavior can be improved by adjusting the weighting parameters in the LQR controller. In Fig. 24 four of the thirteen constituent trajectories are shown to illustrate how the 3D trajectories can differ in the $x - yz$ plane, but their projection onto the $y - z$ plane follows the desired trajectory.

To condense the results for the cost of different maneuvers, Figs. 26-28 display, for different configurations, the number of missions realizable with the calculated ΔV, assuming an electric propulsion system with specific impulse of 3500 s, and fixing the maximum ratio of fuel to total mass at 0.3. The number of maneuvers is increased as relax the quality parameter is relaxed.

Notice however, that there are two unachievable zones. The first one is due to the fact that there is a limitation in the minimum time of the maneuvers given the available thrust of electric propulsion systems. Given the requirements of power of electric

propulsion systems, (in the most recent prototypes the efficiency is 70-80mN/KW,[24] and the presently available power sources with specific power of 200kW/Kg[20]), the max acceleration of the system is limited by the fraction of the mass of the power source relative to the mass of the spacecraft. Assuming a value of 25% of the mass to be power generation, the limit in the accelerations of the spacecraft are about 4.5 mm/s^2. Given this limiting value the minimum time of maneuver as well as the minimum value for $\bar{\bar{\Delta}}$, and Q, can be calculated from Eq.(9) and (14), assuming continuous maximum thrust during the whole maneuver, for deep space dynamics (as a lower boundary):

$$T \quad = \quad \int_{R_{min}}^{R_{max}} \frac{dr}{v_r(r)} \tag{5.19}$$

$$= \quad \int_{R_{min}}^{R_{max}} \frac{dr}{\sqrt{a_{max}^2 k^2/\sqrt{r^2 + 4k^2}}}, \tag{5.20}$$

and

$$\bar{\bar{\Delta}}_{min} \quad = \quad \sum_{i=1}^{N_R} \alpha_i \beta_i \frac{1}{\sqrt{a_{max}^2 k^2/\sqrt{1 + 4k^2}}} \tag{5.21}$$

The results are shown in table II. Notice how the minimum time reduces with the reduction of the resolution requirements, and increase in the number of spacecraft. If the acceleration constraint is relaxed, solutions for faster maneuvers are found, but the system is not able to follow them. Fig. 25 shows the effect of the saturation of the control in the trajectories for a 45 minutes, 11 spacecraft maneuver.

On the other side, the maximum value of Q, i.e. highest quality achievable, is also constrained by the time of the maneuver, for a given time of maneuver, there is a limit in the minimum velocity, and so, this limits the quality achievable. The two unachievable regions are clearly depicted in Figs. 26-28. The optimization problem and the LQR are normalized, such that the total cost obtained is directly proportional to

Table II. Minimum time and minimum quality given acceleration constraints $a_{max} = 4.5mm/s^2$

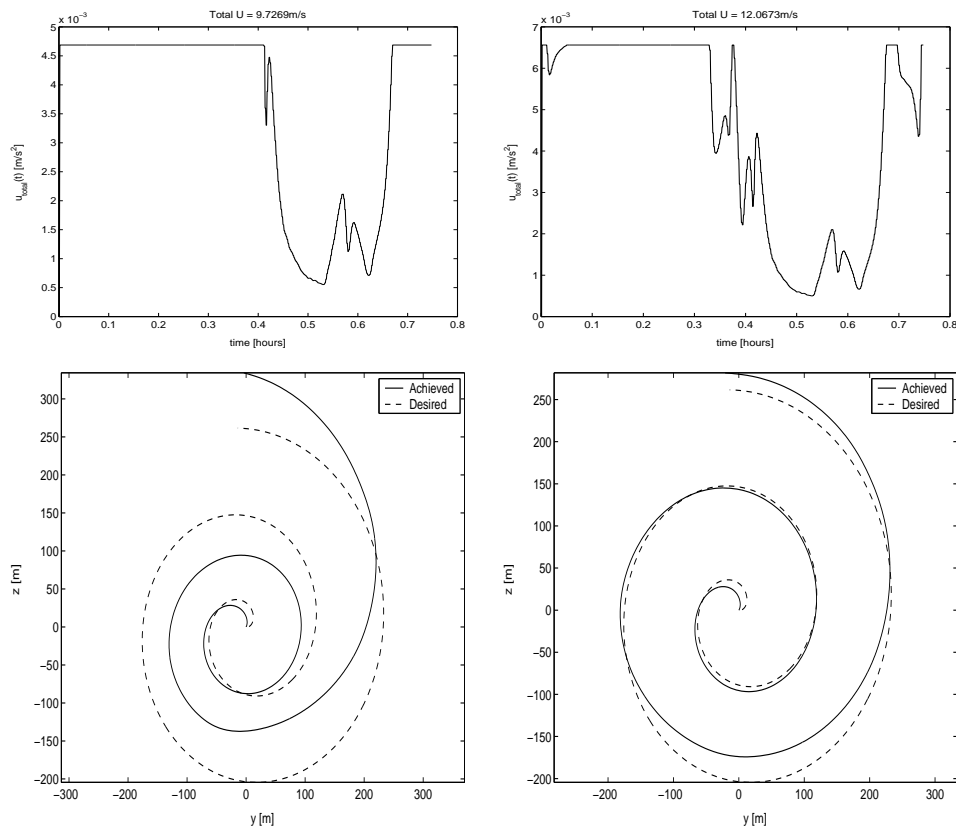| n_s	50 pix			100 pix		
	min time	min Qd	min Qh	min time	min Qd	min Qh
	[h]	$\times 10^5$	$\times 10^5$	[h]	$\times 10^5$	$\times 10^5$
9	0.51	7.77	7.54	0.97	3.78	3.67
11	0.42	6.08	9.21	0.80	2.96	4.49
13	0.37	4.99	10.9	0.68	2.43	5.30

Fig. 25. Control saturation effect in the trajectory tracking, 45 minutes maneuver, 11 spacecraft Left: $a_{max} = 4.7mm/s^2$, Right: $a_{max} = 6.5mm/s^2$
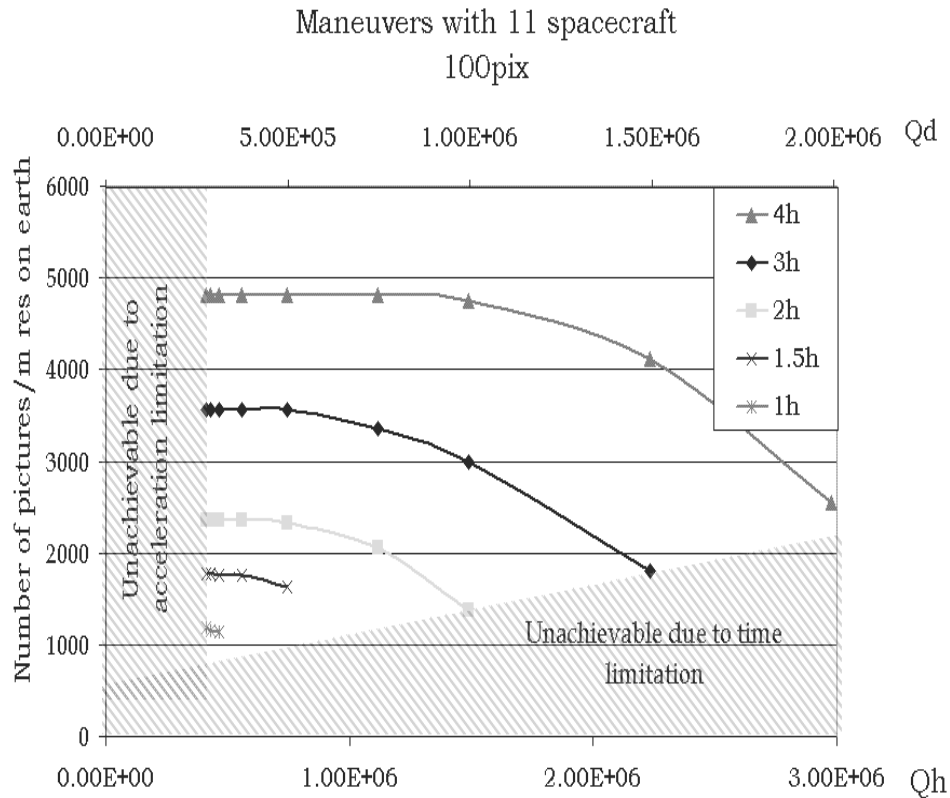
Fig. 26. 11 spacecraft maneuver, 100×100 *pix*. Number of pictures vs. quality (Qd = direct interferometry, Qh = heterodyne interferometry)

the radius of maneuver, and therefore the number of missions is directly proportional to the resolution on earth. The number of pixels in the image is also an important factor in the fuel cost. The number of pictures in Figs. 26-28, are given per meter of resolution desired on the target. The reduction of the number of pixels per picture, means a less tight spiral maneuver and consequently less consumption of fuel. This can be noticed in Fig. 28 that is calculated for a $50 \times 50pix$ images.
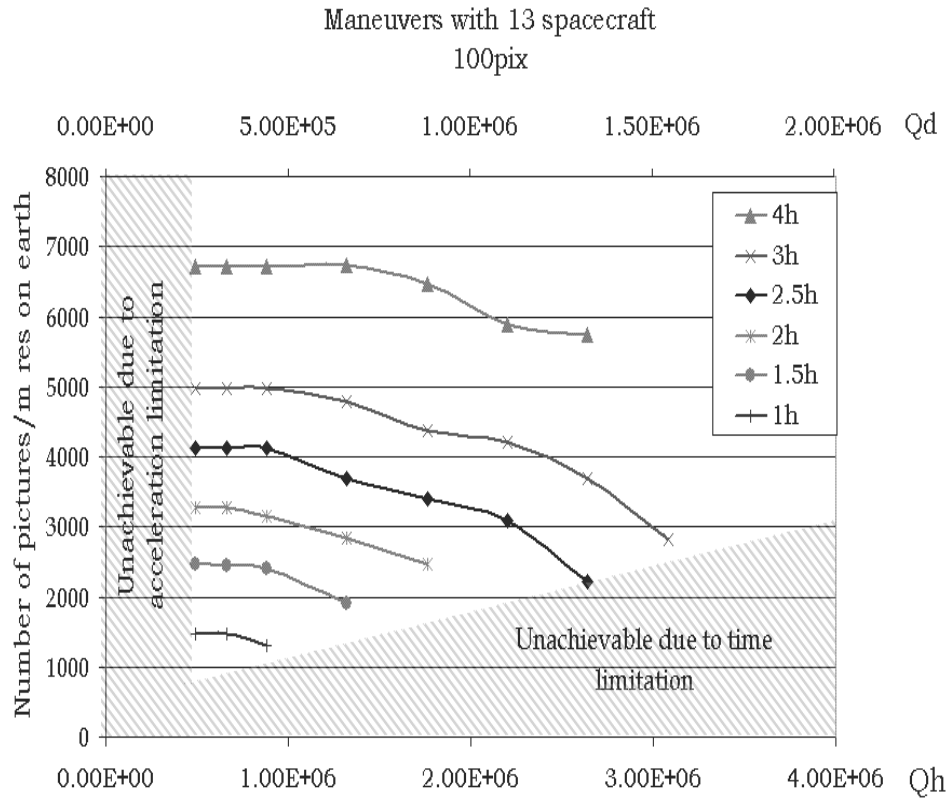
Fig. 27. 13 spacecraft maneuver, 100×100 *pix*. Number of pictures vs. quality (Qd = direct interferometry, Qh = heterodyne interferometry)
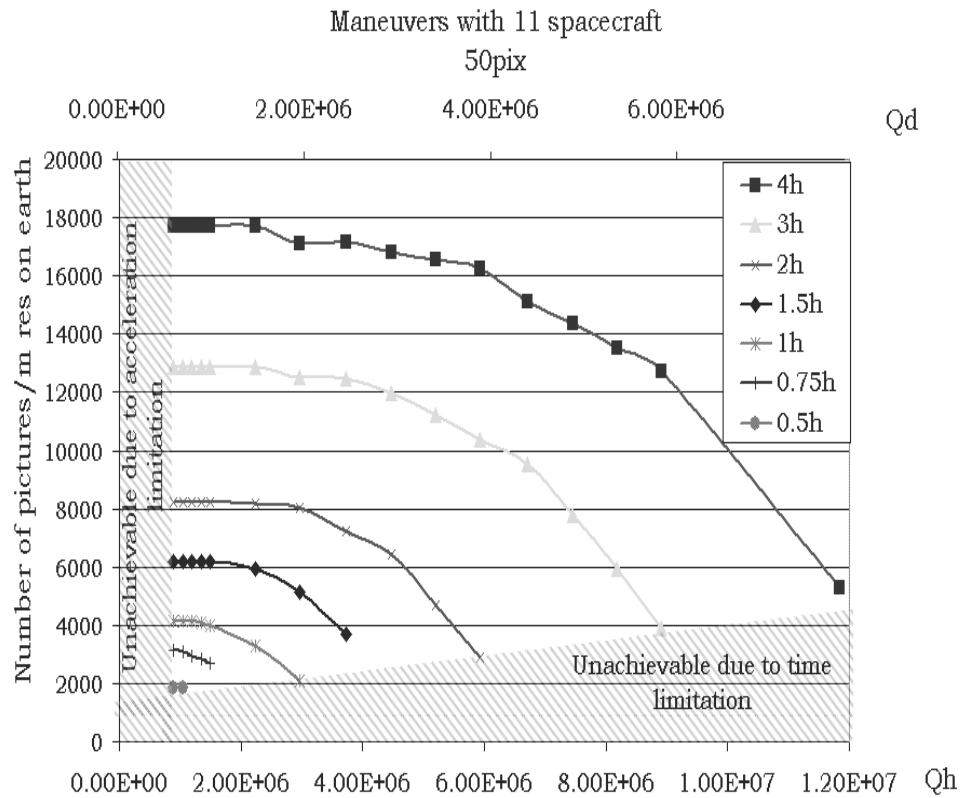
Fig. 28. 11 spacecraft maneuver, 50×50 *pix*. Number of pictures vs. quality (Qd = direct interferometry, Qh = heterodyne interferometry)

CHAPTER VI

NON-STATIC TARGET LOCATION

In the solution stated in the previous chapter, the proposed algorithm assumes that the distance, as well as the relative direction to the target is non varying. Such assumptions are appropriate in the case for example of static objects on earth imaged from a formation in GEO orbit, or the imaging of a distant planet from an orbital location.

However, when the relative position of the target to the formation is varying; as for example in the imaging of an earth based target from a non-GEO location, imaging a near earth object from another near earth orbit, or a moving object on earth; new challenges in the solution of the problem arise. The two stage controller presented in the previous section is extended for this case in the development below.

A.   Time-Varying Direction

When the distance vector to the target is changing direction with time, the actual trajectories of the spacecraft have to be such that they project the trajectories found by the higher level controller, in a plane perpendicular to the optical axis. This plane is changing direction as the relative position changes.

The solution to this problem is achieved defining a time varying observation matrix C that projects the trajectories in the rotating observation plane, and allows for the LQR controller to track the optimal solution found from the first stage. Thus

the LQR controller, is designed for the state space system:

$$\dot{\mathbf{x}} = A\mathbf{x} + B\mathbf{x} \tag{6.1}$$

$$\mathbf{y} = C(t)\mathbf{x} \tag{6.2}$$

being $\mathbf{x}$ the position-velocity vector defined in the local horizontal local vertical (LHLV) reference frame of the system reference circular trajectory, denoted by $\{N\}$, and in the observation equation, $C(t)$ is a time varying matrix that is assumed known from the system and target location. This observation equation defines the yz projection of the trajectories in a rotating coordinate frame.

The reference frame configuration for a general case is shown in Figure 29. The reference frame $\{A\}$ is defined with the $^A x$ axis in the direction of the optical axis. That is, it is defined by a rotation of an angle θ_3 about the $^N z$ axis, and an angle θ_2 about the $^A y$ axis of the N reference frame.

The velocities are defined in the new coordinate frame using the transport theorem:

$$\frac{^N d\mathbf{x}}{dt} = \frac{^A d\mathbf{x}}{dt} + (\omega_{A/N} \times \mathbf{x}) \tag{6.3}$$

Thus:

$$C(t) = [P_{zy}] \begin{bmatrix} R_2 & {}^3 0 \\ {}^3 0 & R_2 \end{bmatrix} \begin{bmatrix} R_3 & {}^3 0 \\ {}^3 0 & R_3 \end{bmatrix} \begin{bmatrix} {}^3 I & {}^3 0 \\ \omega_{N/A}^{\times} & {}^3 I \end{bmatrix} \tag{6.4}$$

$$= \begin{bmatrix} 0\ 1\ 0\ 0\ 0\ 0 \\ 0\ 0\ 1\ 0\ 0\ 0 \\ 0\ 0\ 0\ 0\ 1\ 0 \\ 0\ 0\ 0\ 0\ 0\ 1 \end{bmatrix} \begin{bmatrix} R_2 R_3 & {}^3 0 \\ R_2 R_3 \left[\omega_{N/A}^{\times}\right] & R_2 R_3 \end{bmatrix} \tag{6.5}$$
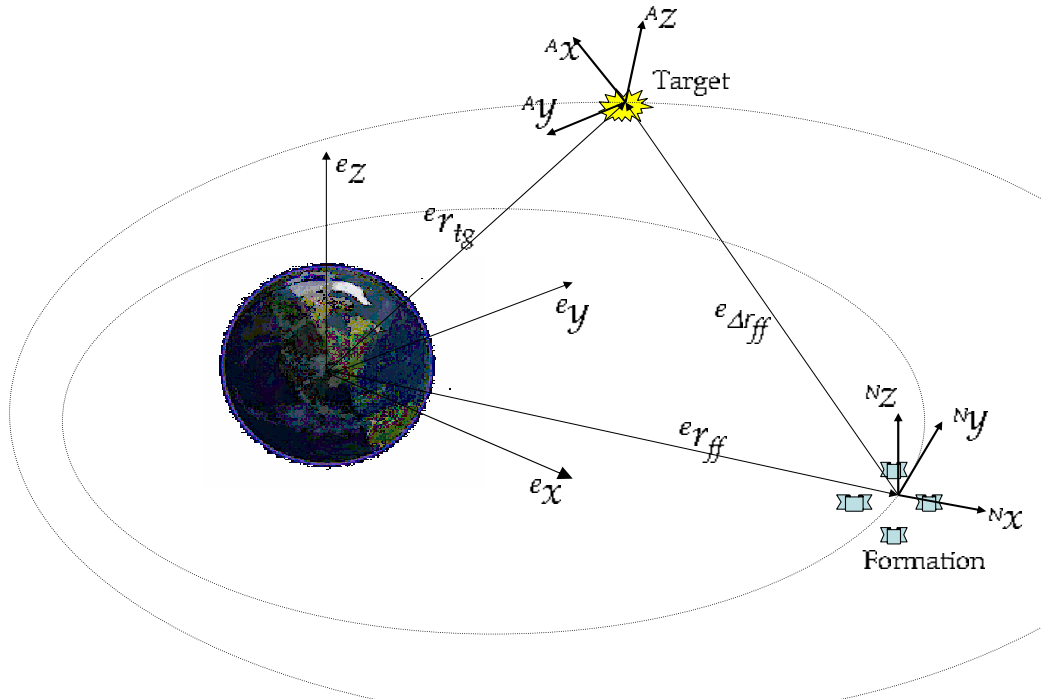
Fig. 29. Coordinate frames

where ^3I and ^{30} are the identity and zeros three dimensional matrices respectively, $R_2(t)$ and $R_3(t)$ are three dimensional rotation matrices that define the rotation of the optical axis with respect to the x direction of the coordinate frame fixed in the LHLV reference frame, P_{yz} is the projector matrix and $\left[\omega_{N/A}^{\times}\right]$ is the skew symmetric matrix for the angular velocity of the frame A relative to N defined in the N frame.

This way, the LQR is actively controlling four constraints in the six dimensional state space $\mathbf{x} = [x, y, z, \dot{x}, \dot{y}, \dot{z}]$. These constraints are defined by the tracking of the reference solution by the projection of the trajectories in the yz plane of the $\{A\}$ frame. The tracking of these constraints attains the satisfaction of the kinematic requirements in the u-v plane that define a bound in the image error content.

Figure 30 shows an example of trajectories found using this algorithm for a simple case where the optical axis is rotating about the z axis. The top figure shows the

trajectories as seen in the LHLV frame. The second plot shows the trajectories in the rotating frame, while the projections of these trajectories on the yz plane are shown in the third figure. The dotted lines are the desired trajectories tracked by the outer loop. The accelerations and the tracking of the reference are shown in the bottom.

B. Time-Varying Relative Distance

When the relative distance to the target is changing, the footprints of the telescopes in the u-v plane, are time varying. In this case, the solution for the higher level controller loses validity, and a new solution to the problem has to be formulated. In Fig. 31, the situation is shown for a case where the target is going away from the imaging system.

The distance from the footprint disc on the u-v plane to the origin, as seen in Fig. 31 is given by:

$$u = \frac{\Delta r_{nm}}{\lambda z}, \tag{6.6}$$

z being the magnitude of the distance from the target to the system. So as z varies with time, the relative distances of the spacecraft should compensate for the variations in order to maintain adequate coverage in the u-v plane. Additionally, the size of the discs is also inversely proportional to the distance of the observation plane to the target, such that the expansion rate constraint takes a new form.

In order to formulate a new solution to the problem that accounts for the effects of a time varying z process, the influence of these two effects in the optimal problem formulation has to be studied.
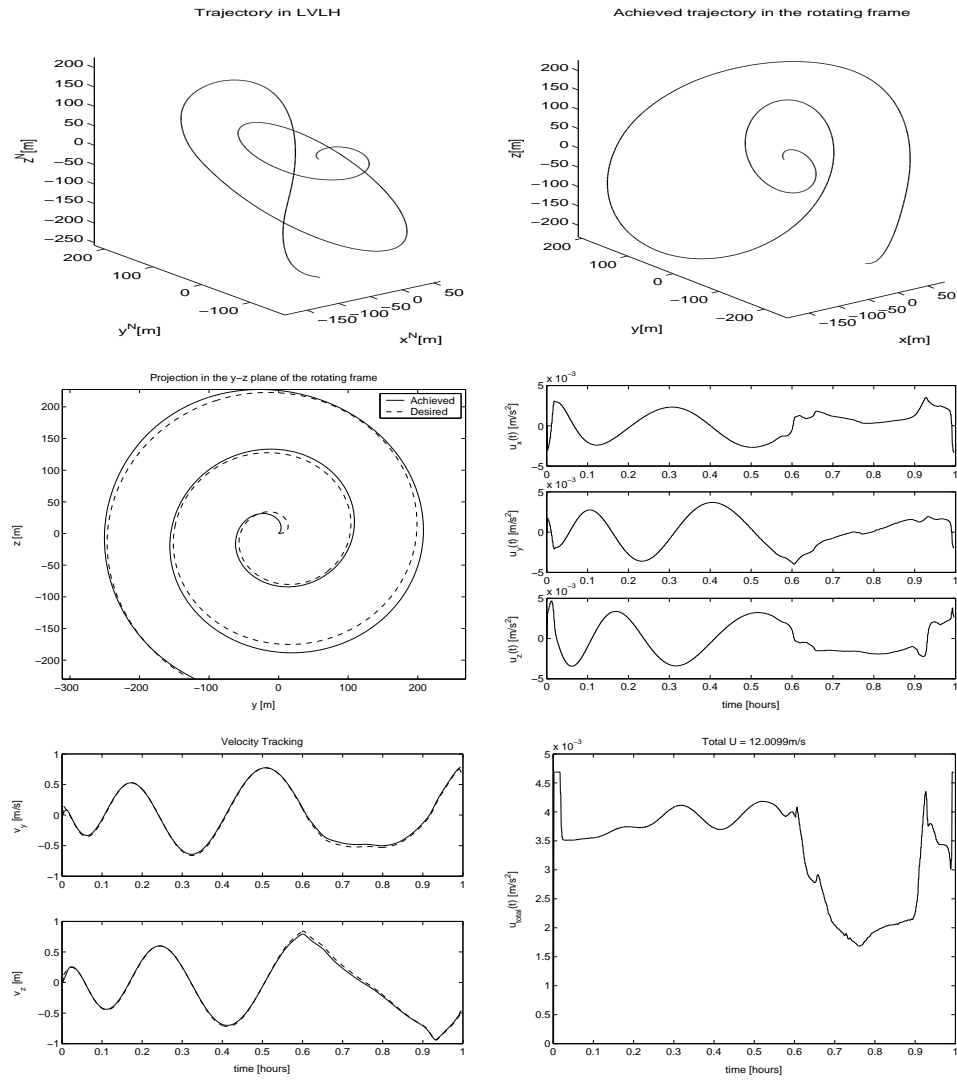
Fig. 30. Maneuver in a frame rotation about θ_3. 11spacecraft, T= 1 h.
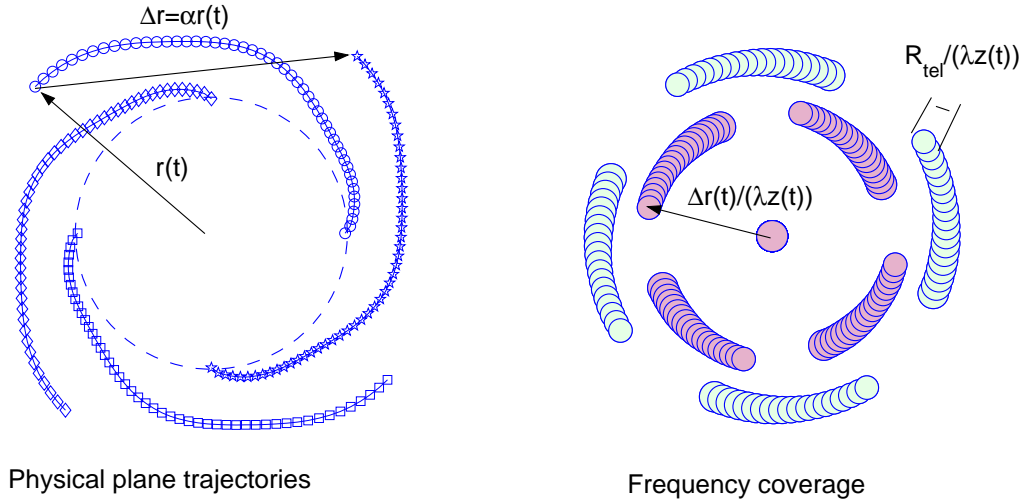
Fig. 31. Relation between the physical plane and the coverage of the u-v plane.

1. Time -Varying Distance in the u-v Plane

In order to comply with the FPC it is necessary to describe a spiral in the u-v plane, defined by the parameters $v_\nu = \frac{dr_\nu}{dt}$, $k_\nu = \frac{dr_\nu}{d\theta}$ that satisfies the imaging constraints. The transformation between the relative positions in the physical plane and the position of the discs in the u-v plane is given by:

$$|\Delta r| = \lambda z(t) r_\nu \qquad (6.7)$$

$$\angle \Delta r = \angle r_\nu \qquad (6.8)$$

where $r_\nu = |\nu|$. Then:

$$k = \alpha \frac{dr}{d\theta} \qquad (6.9)$$

$$= \alpha \frac{d\lambda z(t)\nu}{d\theta} \qquad (6.10)$$

$$= \alpha \lambda z(t) \frac{d\nu}{d\theta} \qquad (6.11)$$

$$= \alpha \lambda z(t) k_\nu \qquad (6.12)$$

where $|\Delta r| = \alpha r$, k_ν is the rate of expansion of the spiral in the u-v plane, and k is the expansion rate for the trajectory in the physical space. And:

$$v_r = \frac{d\lambda z(t)\nu}{dt} \tag{6.13}$$

$$= \frac{d\lambda z(t)}{dt}\nu + \lambda z(t)\frac{d\nu}{dt} \tag{6.14}$$

$$v_r = \lambda \dot{z}(t)\nu + \lambda z(t)v_\nu \tag{6.15}$$

where v_ν is the radial velocity of the spiral in the u-v plane, and v_r is the radial velocity of the trajectory in the physical space.

The cost function is then given by:

$$J = \int_{R_{min}}^{R_{max}} |\mathbf{a}|dt \tag{6.16}$$

$$= \int_{R_{min}}^{R_{max}} |\mathbf{a}|\frac{1}{v_\nu}dr_\nu \tag{6.17}$$

$$= \int_{R_{\nu min}}^{R_{\nu max}} |\bar{\mathbf{a}}_\nu|dr_\nu, \tag{6.18}$$

where,

$$|\bar{\mathbf{a}}_\nu| = |\frac{\mathbf{a}_\nu}{v_\nu}| \tag{6.19}$$

$$= \sqrt{\left(\frac{dv_r}{dr_\nu} - \frac{v_r r}{k^2}\right)^2 + \left(\frac{d}{dr_\nu}\left(\frac{v_r r}{k}\right) + \frac{v_r}{k}\right)^2}, \tag{6.20}$$

such that the cost function can be written as a function only of the elements k_ν, r_ν, v_ν describing the motion in the u-v plane, and the prescribed functions of time $Z(t) = \lambda z(t)$ and $\dot{Z}(t) = \lambda\frac{dz(t)}{dt}$. This allows to define the optimization problem such that it constraints on the spiral are defined in the u-v plane, but the cost function calculates the acceleration in the physical plane.

When the system is discretized, as a function of the radial distance in the u-v

plane $r_\nu^{(i)}$, $i = 1, \ldots, N$ the cost can be calculated as:

$$
J = \sum_{i=1}^{i=N-1} \left[\left(\frac{Z^{(i+1)}v_\nu^{(i+1)} - Z^{(i)}v_\nu^{(i)} + \dot{Z}^{(i+1)}r_\nu^{(i+1)} - \dot{Z}^{(i)}r_\nu^{(i)}}{Z^{(i)}\delta r_\nu} - \frac{Z^{(i)}v_\nu^{(i)}\nu^{(i)} + \dot{Z}^{(i)}r_\nu^{(i)}}{Z^{(i)}\left(k_\nu^{(i)}\right)^2} \right)^2 + \right.
$$
$$
\left. + \left(\frac{(Z^{(i+1)}v_\nu^{(i+1)} + \dot{Z}^{(i+1)}r_\nu^{(i+1)})r_\nu^{(i+1)}}{Z^{(i)}\delta r k_\nu^{(i+1)}} - \frac{(Z^{(i)}v_\nu^{(i)} + \dot{Z}^{(i)}r_\nu^{(i)})r_\nu^{(i)}}{Z^{(i)}\delta r_\nu k_\nu^{(i)}} + \frac{Z^{(i)}v_\nu^{(i)}\dot{Z}^{(i)}r_\nu^{(i)}}{Z^{(i)}k_\nu^{(i)}} \right)^2 \right]^{1/2}
$$

$$(6.21)$$

where $Z^{(i)} = z(t(r_\nu^{(i)}))$, $v_\nu^{(i)} = v_\nu(r_\nu^{(i)})$. Defining $\Phi = \frac{1}{v_\nu\left(\frac{r_\nu}{\alpha_N}\right)}$, the constraints remain the same as stated for the static target problem, in Equations 4.19-4.21

When including these terms, the convexity of the optimization function and the convergence to a global minimum is not guaranteed. However, $Z(t)$ is a well behaved function, at least L_2, and for different initial conditions and different parameters, the optimization converged.

2.   Change in the Footprint Size

When the variation of the distance to the object is negligible as assumed in the previous sections, the footprint of the telescopes in the u-v plane is a disc of constant radius:

$$
\rho = \frac{R_{tel}}{\lambda \bar{z}} \tag{6.22}
$$

where R_{tel} is the radius of the telescope. Then, the maximum value of the spiraling rate k can be calculated such that the size of the discs just overlap while the spiral is expanding.

In the case where z is not a constant, the size of the discs will be time varying, and the above mentioned definition of k_{max} is not valid.

A calculation in the limiting value of k, such that there are no gaps in the coverage

is defined by the constraint:

$$\int_{\theta}^{\theta+\Delta\theta} k d\theta' = \rho(\theta) + \rho(\theta + \Delta\theta) \tag{6.23}$$

This constraint assures that the disc of the spacecraft at θ will arrive just at the border of the coverage of the previous spacecraft at radius $r = r_1$ that is shifted an angular distance $\Delta\theta$.

When differentiating with respect to θ:

$$\frac{d}{d\theta}\left(\int_{\theta}^{\theta+\Delta\theta} k d\theta'\right) = \frac{d}{d\theta}\left(\rho(t(\theta)) + \rho(t(\theta + \Delta\theta))\right) \tag{6.24}$$

$$k(\theta + \Delta\theta) - k(\theta) = \frac{d\rho(t(\theta))}{dr}\frac{dr}{d\theta} + \frac{d\rho(t(\theta + \Delta\theta))}{dr}\frac{dr}{d\theta}$$

$$= \dot\rho(t(\theta))\frac{dt}{dr}k(\theta) + \dot\rho(t(\theta + \Delta\theta))\frac{dt}{dr}k(\theta) \tag{6.25}$$

That is:

$$\frac{d\theta}{dr}(\theta + \Delta\theta) - \frac{d\theta}{dr}(\theta) = \frac{\dot\rho(t(\theta))}{v_r(r(\theta))}k(\theta) + \frac{\dot\rho(t(\theta + \Delta\theta))}{v_r(r(\theta))}k(\theta) \tag{6.26}$$

$$\frac{d\theta}{dr}(\theta + \Delta\theta) = \frac{d\theta}{dr}(\theta)\left(1 + \frac{\dot\rho(r(\theta)) + \dot\rho(r(\theta + \Delta\theta))}{v_r(r(\theta))}\right) \tag{6.27}$$

where $\dot\rho(r)$ and $v_r(r)$ are know functions for a given iteration of $v_r(r)$ in the nonlinear programming problem.

Solving this delay differential equation would require the definition of a computationally expensive solution method.

However, a conservative solution that will guarantee the satisfactory coverage can be defined as follows:

$$k_{max} = min\{\kappa_n, \kappa_{n+1}, ...\}, \quad \forall i = 1, 2, \ldots \quad 0 \leq \kappa \tag{6.28}$$

where:

$$\kappa_n = \frac{\delta r_n}{(\delta \theta)_n} \tag{6.29}$$

defining:

$$\delta r_n = \rho(r) + \rho_{min} - ndr \tag{6.30}$$

$$\delta \theta_n = \Delta \theta - dr \sum \frac{1}{k^{(i-n)}} \tag{6.31}$$

being $\Delta \theta$ the angular separation between spacecraft, which is constants during the maneuver, δr is the discretization size of r, $\rho(r)$ is the radius of the coverage disc at the radial distance r, and ρ_{min} is the smallest value of ρ throughout the maneuver.

When defining k_{max} using this criterium, it is guaranteed that the mth spacecraft will arrive to the r_i radial position just ρ_{min} distance outside of the coverage disc of the $m+1^{th}$ spacecraft, thus allowing for the coverage of the u-v plane without leaving any gaps. Figure 32 shows a plot of r as a function of θ describing the calculation of $k_{max}^{(i)}$.

C. Application: Orbit to Orbit Imaging

To apply this methodology to the case of moving targets, the relative orientation of the spacecraft formation with respect to the target, for different orbital parameters, was computed using Lagrange Generating Functions[25]

The value of z is calculated as the distance from the near-circular reference orbit of the formation to the orbital location of the target:

$$\Delta r = {}^e r_{tg} - {}^e r_{ff} \tag{6.32}$$

$$= ({}^e x_{tg}, {}^e y_{tg}, {}^o z_{tg}) - ({}^e x_{ff}, {}^e y_{ff}, {}^e z_{ff}) \tag{6.33}$$
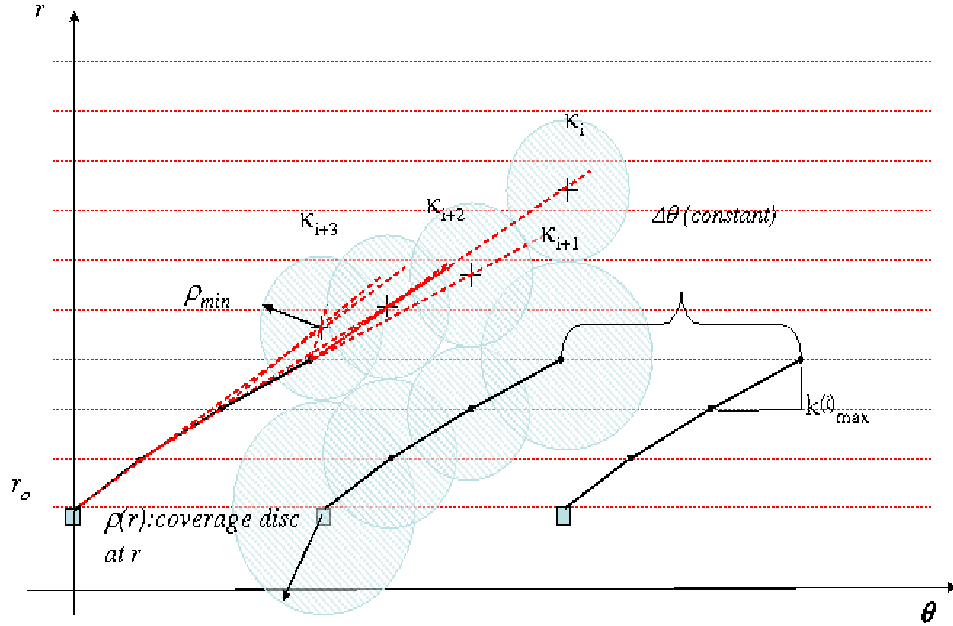
Fig. 32. Definition of $k_{max} = min\{\kappa_i\}$

where r_{tg} is the location of the target, and r_{ff} is the location of the reference origin of the spacecraft formation in the Center of Earth (COE) reference frame e, as shown in fig. 29. The angles of the rotation matrix are obtained by the rotation of the x axis toward the location of the target:

$$\theta_2 \;=\; -\sin^{-1}\left(\frac{\Delta z}{|\Delta r|}\right) \tag{6.34}$$

$$\theta_3 \;=\; \theta_\Delta - \theta_{ff} \tag{6.35}$$

$$\;=\; \tan^{-1}\left(\frac{\Delta y}{\Delta x}\right) - \tan^{-1}\left(\frac{y_{ff}}{x_{ff}}\right); \tag{6.36}$$

Differentiation the above equations

$$\dot{\theta}_2 = \frac{|\dot{\Delta r}|\Delta z - \Delta v_z |\Delta r|}{\Delta r^2 \cos\theta_2} \tag{6.37}$$

$$\dot{\theta}_3 = \frac{\cos^2\theta_\Delta(\Delta v_x \Delta y - \Delta v_y \Delta x)}{\Delta y^2}$$

$$- \frac{\cos^2\theta_{ff}(v_{xff}y_{ff} - v_{yff}x_{ff})}{y_{ff}^2}; \tag{6.38}$$

where

$$|\Delta r| = \sqrt{\Delta x^2 + \Delta y^2 + \Delta z^2}, \tag{6.39}$$

$$|\dot{\Delta r}| = \frac{1}{\Delta r}(\Delta x \Delta v_x + \Delta y \Delta v_y + \Delta z \Delta v_z) \tag{6.40}$$

And the angular velocity of the rotation of the frame is given by:

$$\omega = \dot{\theta}_2 {}^N\hat{z} + \dot{\theta}_3 {}^A\hat{y} \tag{6.41}$$

$$= \dot{\theta}_2 {}^N\hat{z} + \cos\theta_3 \dot{\theta}_3 {}^N\hat{y} - \sin\theta_3 \dot{\theta}_3 {}^N\hat{x} \tag{6.42}$$

D.   Simulations and Results

Different cases for the application of this design methodology were simulated, and the cost of the near fuel optimal maneuver and the magnitude of the controls required were obtained. An arbitrary image quality factor was chosen for the simulations in order to make the imaging constraint active, and the maximum time of maneuver was selected to be 1 hour, using 7 spacecraft and 11 spacecraft. The nominal angular resolution of the optical system used is $\mathcal{R} = \lambda/200m$. The cost of the maneuver is inversely proportional to this parameter and can be estimated for other values.

As a first example, the image of a GEO located spacecraft from a LEO located system is calculated. As a second example, the system is simulated to image a LEO located target from another LEO location. As a third case a similar maneuver but

using 11 spacecraft is shown. As a fourth case, an imaging maneuver from LEO to an earth based target is calculated. And, the last case, assumes an imaging maneuver from LEO located system to a target in a HEO orbit at 12500 km. The arbitrary selected orbital parameters for the system reference orbit are: a = 7800 m., e= 0.01. The inclination of the different orbits were arbitrary selected for each case.

Figures 33 to 37, display the results. For the different cases the top-left figure shows the configuration of system and target in the maneuver. The top-right figure shows the value for the distance of the system to the target (z), and the relative angles for the rotation from the optical axis to the x direction in the LHLV , (θ_2, θ_3), as functions of time. In the second row, the left figure show the trajectories as seen in the LHLV reference frame of the system $\{N\}$ and the right side shows the projection of the trajectories in the ^Nyz axis as seen in the optical axis frame $\{A\}$. Notice the expanding rate of the spiral trajectories compensating for the variations of the distance of the target to the system. In cases like the one shown in Fig. 36, it can be seen that the spiral contracts to compensate when the system approaches to the target and then quickly expands to compensate for the increase of this distance. As the distance change over time is smaller, the spiral expansion rate seem more uniform, as is seen in the case of GEO target imaging (see fig.35), where the relative variation is not as large as in the other cases. In the bottom row, the left side shows the total acceleration for all of the spacecraft as a function of time in order to display the required acceleration levels for the system, and in the right side the performance of the tracker is shown following the y and z reference trajectories.

In order to consider the probability of collision, a minimum value for the distance between spacecraft is the distance in the yz plane projection in the A frame. When the spacecraft are following the required trajectories, at any single time, since they will not necessarily lay in the same yz plane, they will be at a relative distance at

least the one defined in the projection. If this fact is considered, it can be noted that the distance between spacecraft has a minimum bound given by the relative distance in the projected spiral.

Since the angular distance between spacecraft in the projected trajectories is a constant, the distance between spacecraft is only proportional to the radial distance. Then, the maximum bound for the probability of collision is proportional to the instant radius of the projected trajectories. By this criteria, the probability of collision is larger at the smallest radius of maneuver, and this happens at the beginning of the maneuver. Thus, controlling the distances at the smallest radial distance of the maneuver is the main concern in the control of collision probability bettween spacecraft.
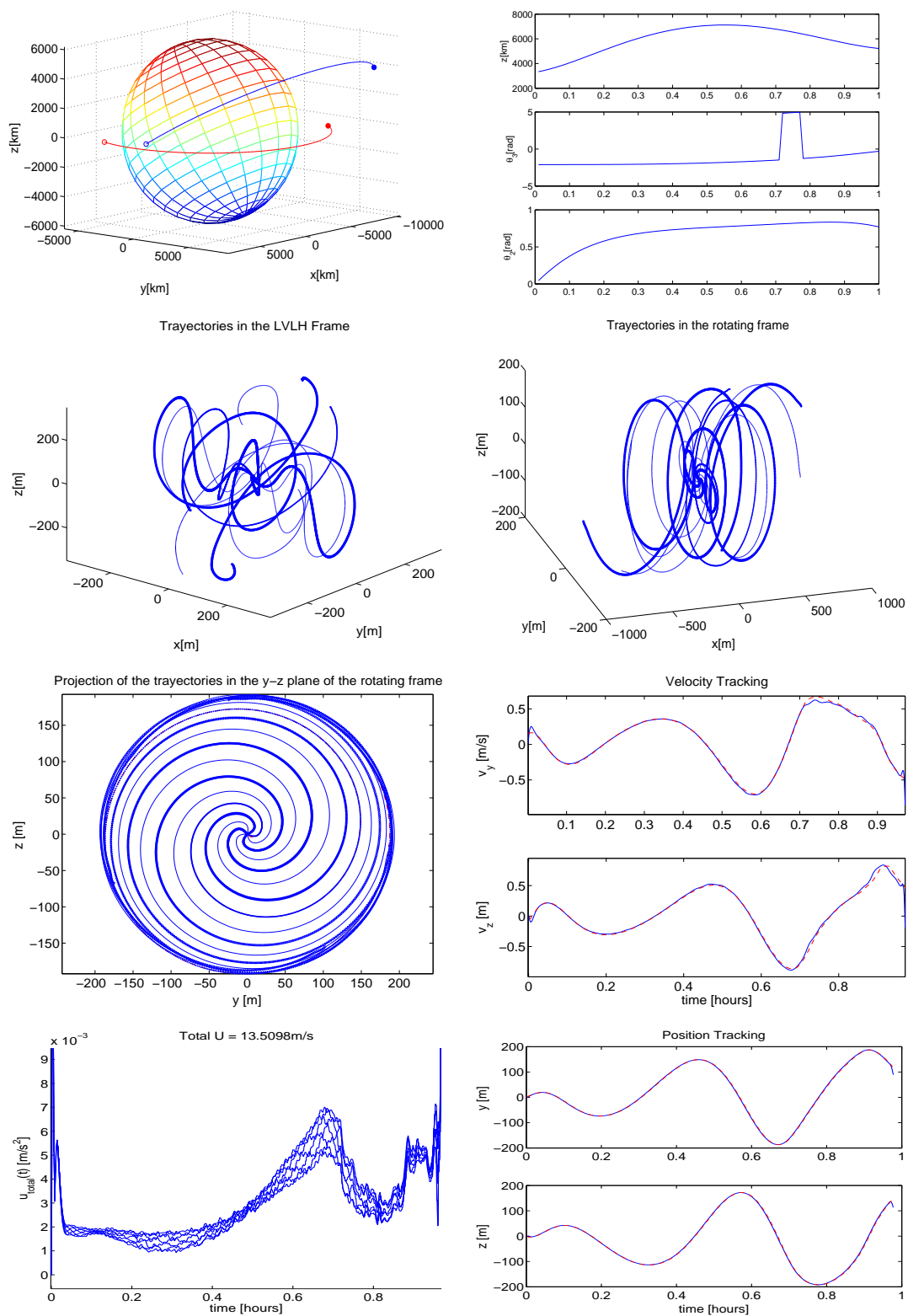
Fig. 33. LEO to LEO imaging maneuver with 7 spacecraft , 1 h,
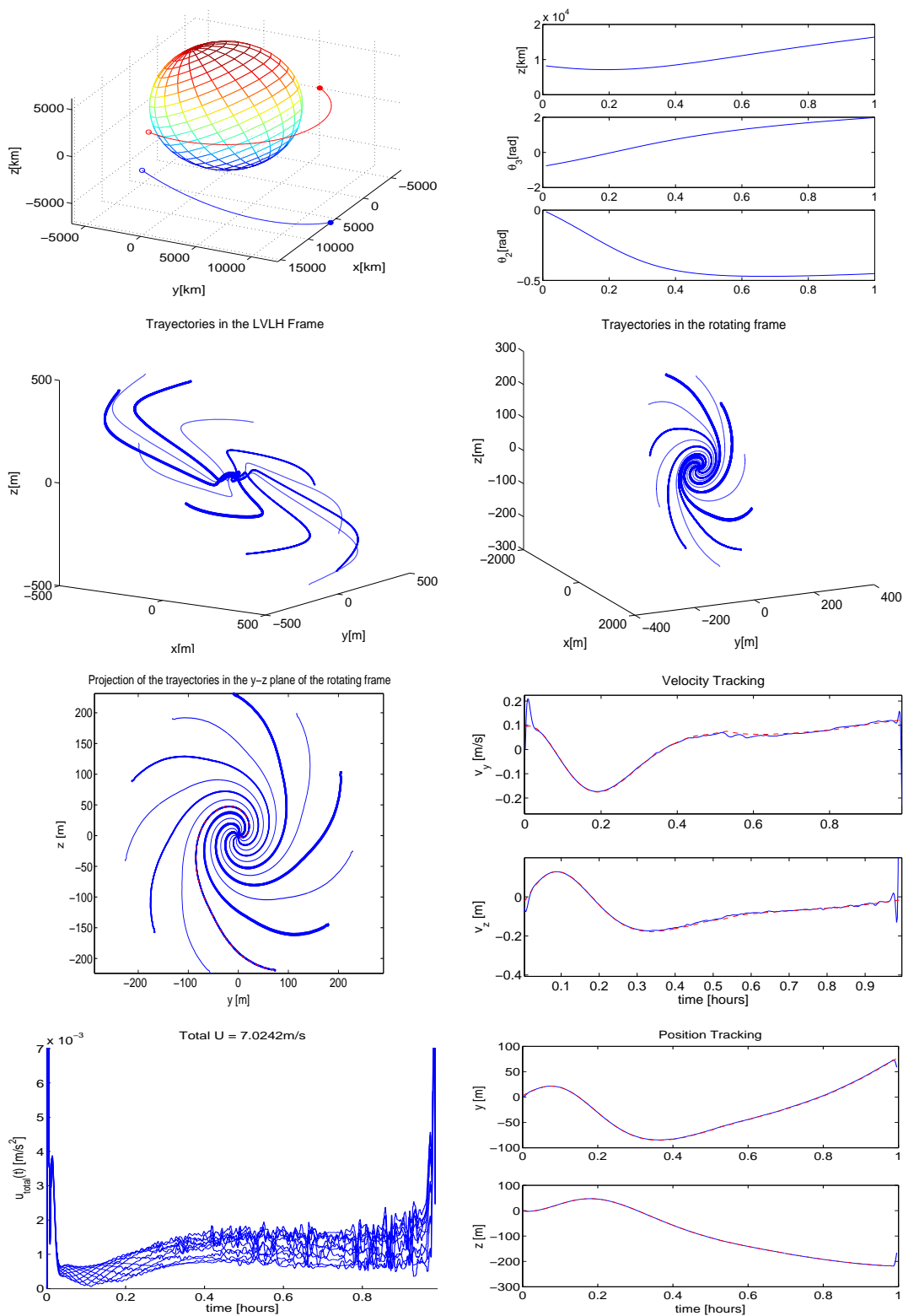
Fig. 34. LEO to LEO imaging maneuver with 11 spacecraft , 1 h,
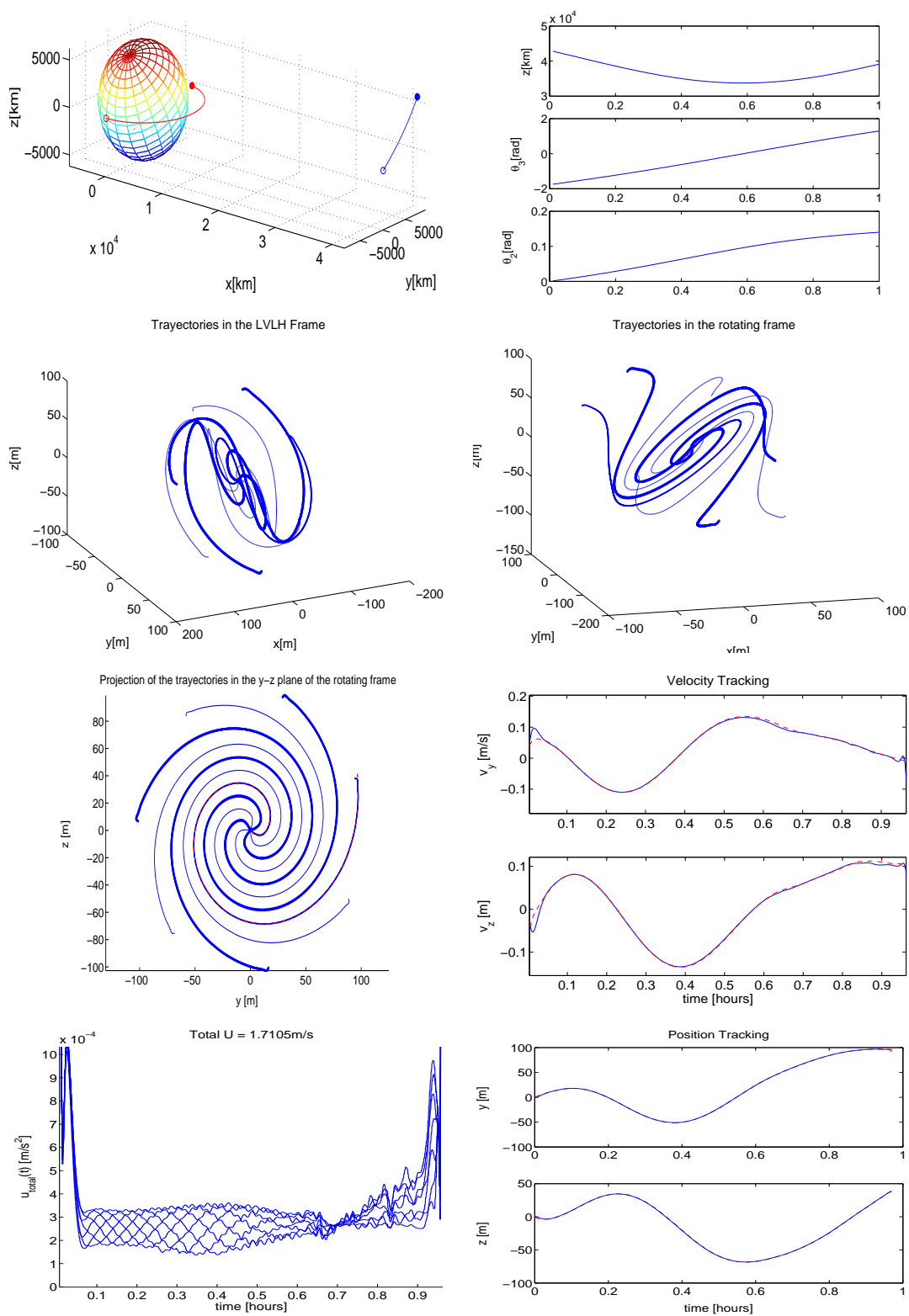
Fig. 35. LEO to GEO imaging maneuver with 7 spacecraft , 1 h,
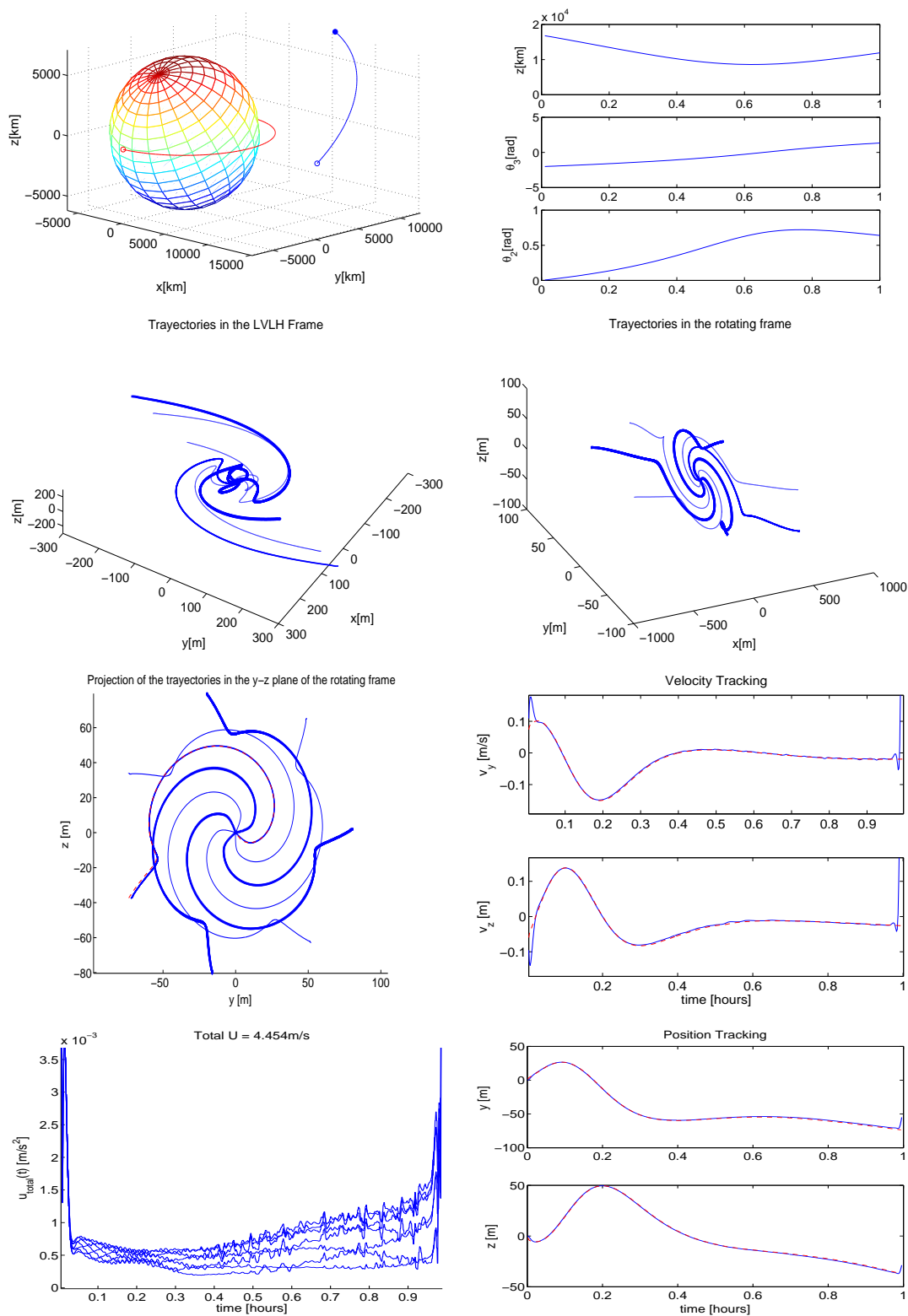
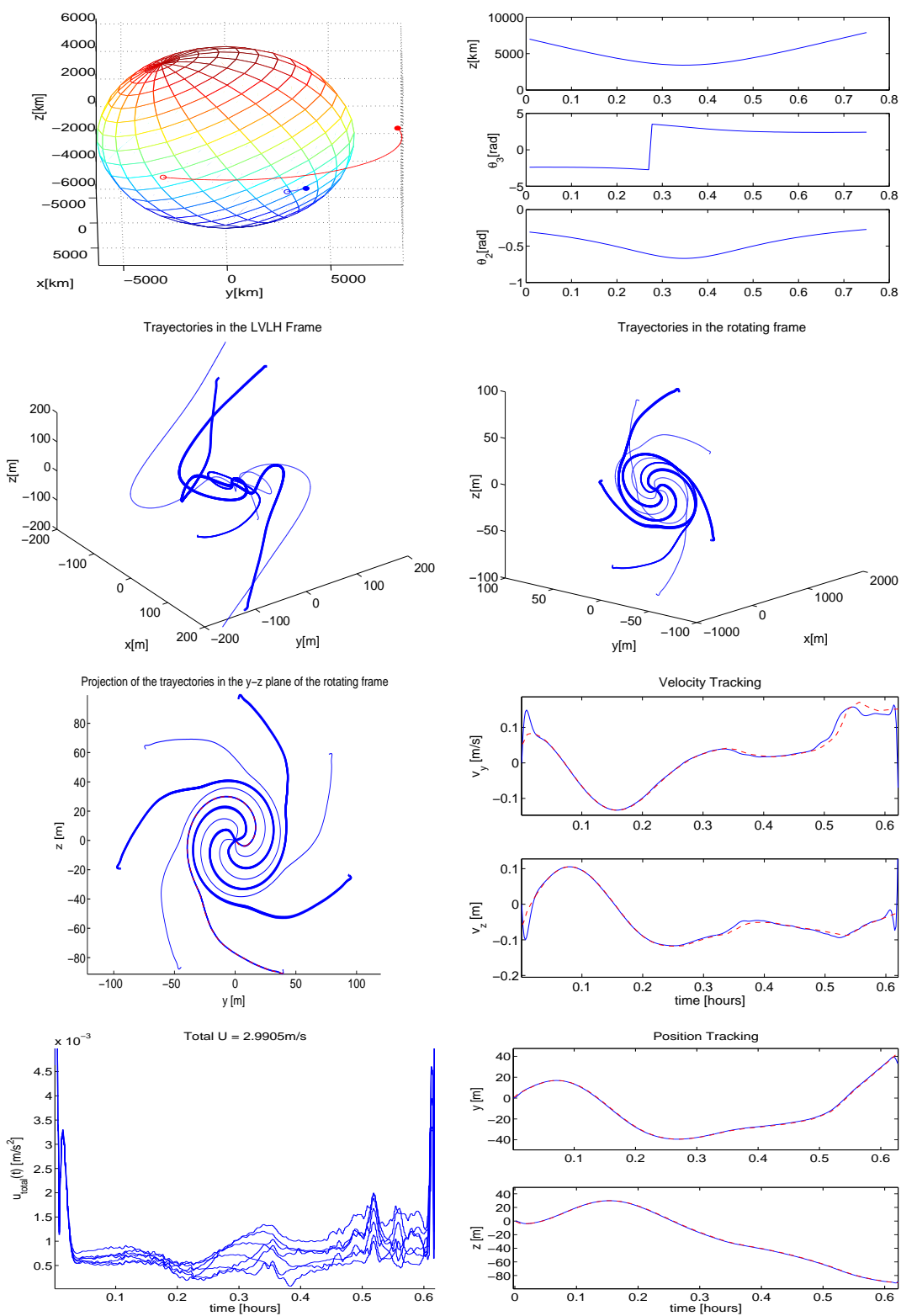Fig. 36. LEO to HEO imaging maneuver with 7 spacecraft , 1 h,

Fig. 37. LEO to EARTH imaging maneuver with 7 spacecraft , 1 h,

CHAPTER VII

CONCLUSIONS

In this research work, a methodology to design optimal trajectories for Multi-Spacecraft Interferometric Imaging Missions has been proposed and using this methodology, the features of such systems have been studied.

The optimization problem can be posed and extended to any number of spacecraft, making use of previous developments and assuming optimality of spiral coverage.

In order to relate the reliability of an image obtained by a given trajectory, relationships between the error in the frequency image and the reliability of the actual image can be defined. Two different measurements of reliability can be considered. First, the probability that any pixel of the image has bounded error, or second, the probability that the total error in the image is bounded. These relationships allow for the definition of the coverage requirement in the maneuver given a requirement in the reliability of the final image.

The optimization problem in the case of deep space dynamics can be converted, under some approximations, to a convex programming problem whose solutions, for different times of maneuver and number of spacecraft, can then be easily obtained.

Further, the problem can be extended to the case with dynamical constraints, like the case of Clohessy-Wiltshire equations of motion for perturbations about a circular orbit. However, the complexity of the problem does not allow for the design of an efficient direct optimization method, and thus, a methodology to find near optimal solutions has been proposed.

An algorithm to calculate near minimum fuel trajectories, consisting of a Sequential Quadratic Programming and a Linear Quadratic Tracker can be used to calculate

near minimum fuel consumption and feasibility of these systems.

As an application, a night IR imager located in GEO was considered. The trajectory design method was used to compute the fuel consumption for various cases, and to relate the fuel requirements to the quality of the pictures.

A two stage hierarchical controller was designed to obtain near fuel optimal trajectories for missions with system-target relative position varying in time. In these missions, many parameters are involved and a tool to design near minimum fuel maneuvers for various different selection of parameters allows for the analysis of the feasibility of such missions. The methodology described in this document allows for the calculation of the dynamic requirements and fuel consumption of near optimal trajectories, accounting for orbital dynamics and the motion of the target, and can be used as such a design tool. The solutions obtained suggest the feasibility of these maneuvers using low thrust engines. These types of maneuvers are flexible enough to image moving targets, different from systems that rely only on passive coverage of the u-v plane. A specific effect that has not yet been acknowledged in this section is the relative attitude change of the target with time. For longer times of maneuver this effect can be a notorious distortion effect in the final picture.

The implementation of these systems in a hybrid multi-satellite system that combines passive and active coverage of the frequency plane could be a further topic of research.

Further considerations that are out of the scope of this work include the attitude control requirement of these systems, the effect of optical aberration, thermal control and higher order gravitational effects not included in the Clohessy-Wiltshire model.

REFERENCES

[1] A. Quirrenbach, "Optical Interferometry," *Annual Review in Astronomy and Astrophysics*, vol. 39, pp 353-401, 2001.

[2] J. W. Goodman, *Introduction to Fourier Optics*, Boston, MA: McGraw Hill, 1996.

[3] C. H. Townes,"Spatial Interferometry in the Mid-Infrared Region," *Journal of Astrophysics and Astronomy*, vol. 5, pp. 111-130, 1984.

[4] S. Chakravorty, P. T. Kabamba and D. C. Hyland "Guaranteed Classification Performance of Multi-Spacecraft Interferometric Imaging Systems," *Journal of the Astronautical Sciences*, vol.51, no. 2, pp. 205-226, 2003.

[5] S. Chakravorty, *Design and Optimal Control of Multi-Spacecraft Interferometric Imaging Systems*, Ph.D. dissertation, Department of Aerospace Engineering, University of Michigan, Ann Arbor, MI, 2004.

[6] S. Chakravorty, P. T. Kabamba and D. C. Hyland, "Modeling of Image Formation in Multi-Spacecraft Interferometric Imaging Systems," *AIAA Space 2004 Conference and Exposition*, vol. 1, pp. 699-720, 2004.

[7] D. C. Hyland, "Entry Pupil Processing Approaches for Exo-Planet Imaging," in*Proceedings of SPIE - The International Society for Optical Engineering*, vol. 5905, pp. 1-18, 2005.

[8] D. C. Hyland, "Constellations Using Entry Pupil Processing for High Resolution Imaging of Geosynchronous Objects," in *Proceedings of the 16th AAS/AIAA Space Flight Mechanics Conference*, AAS 06-230, pp. 1-18, Tampa, FL, 2006.

[9] I. I. Hussein, D. Scheeres and D. C. Hyland, "Interferometric Observatories in Earth Orbit," *Journal of Guidance, Control and Dynamics*, vol . 27, no. 2, pp. 297- 301, 2004.

[10] D. C. Hyland, "Exo-planet Detection Via Stellar Correlation Interferometry,"in *Proceedings of SPIE - The International Society for Optical Engineering* , vol. 5905, pp. 1-17, 2005.

[11] D. P. Scharf, F. Y. Hadaegh, and S. R. Ploen, "A Survey of Spacecraft Formation Flying Guidance and Control. Part II: Control," in *Proceedings of the 2004 American Control Conference*, vol. 4, part 4, pp. 2976-2985, Boston, Jun 2004.

[12] I. I. Hussein, D. Scheeres, and D. C. Hyland, "Control of a Satellite Formation for Imaging Application," in *Proceedings of the American Control Conference*, vol. 1, pp. 308-313, 2003.

[13] E. M. Kong, D. W. Miller and R. J. Sedwick," Exploiting Orbital Dynamics for Aperture Synthesis Using Distributed Satellite Systems: Applications to Visible Earth Imager System," *Journal Astronautical Sciences*, vol. 47, no. 1-2, pp. 53-75, 1999.

[14] A. B. DeCoe," Orbital Station-Keeping for Multiple Spacecraft Interferometry," *Journal of the Astronautical Sciences*, vol. 39, no. 3, pp. 283-297, 1991.

[15] S. Chakravorty, P. T. Kabamba, and D. C. Hyland, "Design of Minimum Time Maneuvers for Multi-Spacecraft Interferometric Imaging Systems," in *Proceedings of the SPIE, Modeling and Systems Engineering for Astronomy*, pp. 427-436, 2004.

[16] S. Chakravorty, P. T. Kabamba and D. C. Hyland, "Design of Minimum Time

Maneuvers for Multi-Spacecraft Interferometric Imaging Systems," *The Journal of the Astronautical Sciences*, vol. 52, no. 3, July-September 2004.

[17] S. Chakravorty, "On the Fuel Optimality of Maneuvers for Multispacecraft Interferometric Imaging systems," in *Proceedings of the AAS/AIAA Space Flight Mechanics Meeting*, AAS 05-159, Copper Mountain, CO, 2005.

[18] J. Ramirez and S. Chakravorty, "Fuel Optimal Spiral Maneuvers for Multispacecraft Interferometric Imaging Systems in Deep Space," in *Proceedings of the AAS/AIAA Space Flight Mechanics Meeting*, AAS 06-164, Tampa, FL, 2006.

[19] J. A. Kong, *Theory of Electromagnetic Waves*. New York: John Wiley and Sons, 1975.

[20] P. Fortescue, J. Stark, and G. Swinerd, *Spacecraft Systems Engineering*, Chichester: John Wiley & Sons, 2003.

[21] H. Schaub and J. Junkins *Analytical Mechanics of Space Systems*. Reston, VA: AIAA Education Series, 2003.

[22] F. Lewis and V. Syrmos, *Optimal Control*. New York: John Wiley and Sons. 1995.

[23] R. Siegel and J. Howell, *Thermal Radiation and Heat Transfer*, 4th Ed. London: Taylor and Francis, 2002.

[24] R. Janosky and S. Tverdokhlebov, "High Power Hall Thrusters," NASA TM - 1999-209436; also AIAA Paper 99-2949. 1999.

[25] R. Battin, *An Introduction to the Mathematics and Methods of Astrodynamics*. Rev. Edition. New York: AIAA Education Series. 1999.

[26] S. Chakravorty and J. Ramirez, "On the Fuel Optimal of Multispacecraft Inter-ferometric Imaging Systems," *Journal of Guidance, Dynamics and Control*, July 2006, in press.

[27] S. Chakravorty and J. Ramirez,"Near Minimum Fuel Spiral Maneuvers for Multi-spacecraft Interferometric Imaging System in Near-Earth Orbit," July 2006, un-publised manuscript.

[28] W. E. Wiesel, *Spaceflight Dynamics*, 2nd Ed., New York: McGraw Hill, 1997.

[29] A. E. Siegman," The Antenna Properties of Optical Heterodyne Receivers," in *Proceedings of the IEEE*, vol. 54 , no. 10. pp. 1350 -1356, 1966.

[30] M. C. Teich, "Infrared Heterodyne Detection," in *Proceedings of the IEEE*, vol. 56, no. 1, pp. 37 - 46, 1968.

[31] B. J. Cooke, W. Smith, B. E. Laubscher, P. V. Villeneuve and S. Briles, "Analysis and System Design Framework for Infrared Spatial Heterodyne Spectrometers," in *Proceedings SPIE Conference on Infrared Imaging Systems* SPIE vol. 3701, Orlando, FL, pp. 167 - 191, 1999.

VITA

Jaime Luis Ramirez Riberos is from Bogota, Colombia where he earned a bachelor's degree in mechanical engineering from Universidad de los Andes in March 2001. His degree project was the design and construction of a 18" slow speed wind tunnel for the Mechanical Engineering Department. In 2002, he had a research internship at the Jefferson Laboratory and obtained a second bachelor's degree in physics, the final project for which focused on chaotic motion of spin controlled satellites. Following undergraduate studies, he spent two years working as a mechanical engineer in the electric generation industry in Bogota. He then took a hiatus in Montpellier, France before enrolling in the master's program in aerospace engineering at Texas A&M in August 2004. His coursework focused on dynamics, optimization and control systems to earn his master's degree in August 2006. As of fall 2006 he will be attending the Massachusetts Institute of Technology pursuing his doctoral studies in the Aeronautics and Astronautics Department.